Progress in Energy

TOPICAL REVIEW • **OPEN ACCESS**

Metallic and complex hydride-based electrochemical storage of energy

To cite this article: Fermin Cuevas *et al* 2022 *Prog. Energy* **4** 032001

IOP Publishing Prog. Energy 4 (2022) 032001 https://doi.org/10.1088/2516-1083/ac665b

Progress in Energy

OPEN ACCESS

RECEIVED
15 December 2021

REVISED
25 March 2022

ACCEPTED FOR PUBLICATION
11 April 2022

PUBLISHED
27 April 2022

TOPICAL REVIEW

Metallic and complex hydride-based electrochemical storage of energy

Fermin Cuevas[1,*], Mads B Amdisen[2], Marcello Baricco[3], Craig E Buckley[4], Young Whan Cho[5], Petra de Jongh[6], Laura M de Kort[6], Jakob B Grinderslev[2], Valerio Gulino[3,6], Bjørn C Hauback[7], Michael Heere[8,9], Terry Humphries[4], Torben R Jensen[2], Sangryun Kim[10,11], Kazuaki Kisu[11], Young-Su Lee[5], Hai-Wen Li[12], Rana Mohtadi[13], Kasper T Møller[14], Peter Ngene[6], Dag Noréus[15], Shin-ichi Orimo[11,16], Mark Paskevicius[4], Marek Polanski[17], Sabrina Sartori[18], Lasse N Skov[2], Magnus H Sørby[7], Brandon C Wood[19], Volodymyr A Yartys[7], Min Zhu[20] and Michel Latroche[1,†]

[1] Univ Paris Est Creteil, CNRS, ICMPE, UMR 7182, UMR7182, Thiais, 94320, France
[2] The Interdisciplinary Nanoscience Center (iNANO) and Department of Chemistry, Aarhus University, Aarhus C, DK-8000, Denmark
[3] Department of Chemistry, NIS and INSTM, University of Turin, Via Pietro Giuria 7, 10125 Torino, Italy
[4] Department of Physics and Astronomy, Curtin University, GPO Box U1987, Perth, WA, 6845, Australia
[5] Center for Energy Materials Research, Korea Institute of Science and Technology, 5 Hwarang-ro 14-gil, Seongbuk-gu, Seoul 02792, Republic of Korea
[6] Materials Chemistry & Catalysis, Debye Institute for Nanomaterials Science, Utrecht University, 3584 CG Utrecht, The Netherlands
[7] Institute for Energy Technology (IFE), 2007 Kjeller, Norway
[8] Institute for Applied Materials—Energy Storage Systems (IAM-ESS), Karlsruhe Institute of Technology (KIT), Hermann-von-Helmholtz-Platz 1, 76344 Eggenstein-Leopoldshafen, Germany
[9] Technische Universität Braunschweig, Institute of Internal Combustion Engines, Hermann-Blenk-Straße 42, 38108 Braunschweig, Germany
[10] Graduate School of Energy Convergence, Gwangju Institute of Science and Technology (GIST), 123 Cheomdangwagi-ro, Buk-gu, Gwangju 61005, Republic of Korea
[11] Advanced Institute for Materials Research (WPI-AIMR), Tohoku University, 2-1-1 Katahira, Aoba-ku, Sendai, Japan
[12] Hefei General Machinery Research Institute, No. 888, Changjiang West Road, Hefei 230031, People's Republic of China
[13] Toyota Research Institute of North America, Materials Research Department, 555 Woodridge Avenue, Ann Arbor, MI, United States of America
[14] Department of Biological and Chemical Engineering, Aarhus University, Aabogade 40, Aarhus DK-8200, Denmark
[15] Department of Materials and Environmental Chemistry, Stockholm University, 106 91 Stockholm, Sweden
[16] Institute for Materials Research, Tohoku University, 2-1-1 Katahira, Aoba-ku, Sendai, Japan
[17] Department of Functional Materials and Hydrogen Technology, Military University of Technology, 00-908 Warsaw, Poland
[18] Department of Technology Systems, University of Oslo, Kjeller, NO-2027, Norway
[19] Laboratory for Energy Applications for the Future (LEAF), Lawrence Livermore National Laboratory, 7000 East Avenue, Livermore, CA 94550, United States of America
[20] South China University of Technology, Guangzhou 510641, People's Republic of China
[†] Deceased.
[*] Author to whom any correspondence should be addressed.

E-mail: fermin.cuevas@cnrs.fr

Keywords: metal and complex hydrides, anodes, electrolytes, batteries

Abstract

The development of efficient storage systems is one of the keys to the success of the energy transition. There are many ways to store energy, but among them, electrochemical storage is particularly valuable because it can store electrons produced by renewable energies with a very good efficiency. However, the solutions currently available on the market remain unsuitable in terms of storage capacity, recharging kinetics, durability, and cost. Technological breakthroughs are therefore expected to meet the growing need for energy storage. Within the framework of the Hydrogen Technology Collaboration Program—H_2TCP Task-40, IEA's expert researchers have developed innovative materials based on hydrides (metallic or complex) offering new solutions in the field of solid electrolytes and anodes for alkaline and ionic batteries. This review presents the state of the art of research in this field, from the most fundamental aspects to the applications in battery prototypes.

1. Introduction

The development of new types of energy storage systems to accommodate the intermittent nature of renewable energy sources is of utmost importance for societal progress towards the sustainable development goals. The commercial lithium-ion battery (LIB) is very successful, but further improvements are incremental, and most battery researchers agree that a completely new technology needs to be developed [1]. Thus, incremental improvement of known materials appears to be insufficient, and the discovery of novel materials may form the basis for technological paradigm shifts. Here, we discuss hydrogen-based materials, which within the past few years received increasing attention for electrochemical energy storage. Novel types of batteries may have extreme societal impact and result in a breakthrough in the transition towards a fossil-free future.

Commercial LIB employ carbonate-based liquid electrolytes which suffer from high flammability and toxicity limiting the safety [2]. Moreover, the liquid electrolytes are incompatible with lithium metal anodes, limiting the energy capacity [3]. The development of novel all-solid-state batteries (SSBs), far beyond the well-known lithium-ion ones, hold a large potential for achieving much higher energy densities, safer, and cheaper batteries and with better performance compared to state-of-the-art LIB [1, 4, 5]. However, the development of new high-performance electrolytes with fast mobility of monovalent as well as divalent cations has been a significant challenge to overcome for the further progress of SSB. Metal hydride electrolytes have recently added new hope to the development of SSB. New types of functional electrolytes may allow new types of electrode materials to be developed and used in future electrochemical cells.

There are several advantages of metal hydride electrolytes. Firstly, the reducing nature of metal hydrides increases the stability towards metal anodes and often allows formation of a stable and conductive interphase [6]. Secondly, complex hydride-based electrolytes often contain a mixed ionic-covalent bonding which results in a very low electronic conductivity. Thirdly, this class of materials has extreme diversity in structures, compositions, and properties, which allow further 'structural and material engineering' and the development of novel materials and nanocomposites. This is illustrated by the discovery of a novel cationic conductivity mechanism based on a flexible network of di-hydrogen bonds, $\mathrm{B{-}H^{\delta-}\cdots{}^{+\delta}H{-}N}$, in the solid-state. This approach is demonstrated both for mono-valent ($\mathrm{Li^+}$) and divalent ($\mathrm{Mg^{2+}}$) fast cationic conductors, such as $\mathrm{LiBH_4{\cdot}0.5NH_3}$ and $\mathrm{Mg(BH_4)_2{\cdot}NH_3}$. Interestingly, the compound $\mathrm{MgCl_2{\cdot}2NH_3}$, which lacks a network of dihydrogen bonds is an insulator. Furthermore, novel types of proton conductors are also discovered, which contain a rare composite ion, $\mathrm{N_2H_7^+}$, i.e. $\mathrm{NH_3{-}NH_4^+}$. However, these ammonium *closo*-borate ammines, such as $\mathrm{(NH_4)_2B_{10}H_{10}{\cdot}}x\mathrm{NH_3}$ ($x = 1/2$, 1 (α and β)) and $\mathrm{(NH_4)_2B_{12}H_{12}{\cdot}}x\mathrm{NH_3}$ ($x = 1$ and 2), contain a large $\mathrm{B}_n\mathrm{H}_n^{2-}$ anion, which limits the proximity of the composite cations and thereby the proton conductivity [7].

In addition to electrolytes, metallic hydrides are also widely used as anodes, at the commercial level for alkaline batteries (NiMH) and at the research state for ion batteries, using a conversion reaction with alkali metals. The first generation of alloys for NiMH anodes was based on AB_5 $\mathrm{LaNi_5}$-type materials (A: rare earth, B: transition elements). Over two decades, they have been developed and fully optimized, leading to complex multi-elemental over-stoichiometric compounds containing more than nine elements [8–10]. NiMH technology remains competitive thanks to its reliability, compactness, safety, and low cost. It is the subject of intense research, particularly in Asia (China, Japan) and Northern Europe. It is positioned in application segments such as small portable electrical equipment (shavers, toothbrushes, tools, etc.), mobility (almost all hybrid vehicles use this type of battery) and stationary applications (security lighting and electricity storage associated with intermittent renewable energy). However, AB_5-type alloys have reached their performance limit and research is now focused on new classes of materials such as superlattice alloys, based on a smart intergrowth between AB_5- and AB_2-type units leading to a very rich chemistry as it allows to play with lighter elements such as magnesium [11]. A step forward has been made by designing rare-earth-free materials and Mg-rich compounds that significantly decrease the molar mass as well as increasing the specific capacities of the anodes.

Besides NiMH battery, the recent discovery of the conversion reaction of metallic hydrides with alkali ions opens new possibilities for the use of these materials as anodes for Li-ion batteries, as they offer high capacities at low potential [12]. The concept has been established in connection with liquid and solid electrolytes, and various compositions have been considered. Most of them are Mg-based materials, but the search for new systems involving 3*d* metals is in progress.

All these newly discovered properties lead to intensive research works in the field of hydride-based electrochemical storage of energy. In the present paper, state-of-the-art results are presented addressing high-capacity anodes, new superionic fast conductors, and full SSBs combining these astonishing materials into practical devices.

2. New high-capacity MH anodes for NiMH aqueous batteries

2.1. Superlattice alloys

AB_5 $LaNi_5$-related intermetallics were successfully applied in the first generation of the alkaline Nickel-Metal Hydrides batteries [13]. While showing robustness and mature performance, their limited electrochemical capacity is a drawback and is restricted by the characteristics of the anode electrode. The reversible hydrogen storage capacity of $\sim$1.10–1.15 wt% H gives 300 mAh g^{-1} during the electrochemical discharge, which is considered insufficient and needs improvements [8].

A more recently developed next generation of anode materials offering an increased discharge capacity exceeding 400 mAh g^{-1} is based on magnesium-containing superlattice type anode electrode alloys. Their intermetallic structures are built from simple and compatible with each other AB_5 Mg-free and AB_2 Mg-rich Laves-type blocks (A: lanthanides) which can be stacked on the top of each other because of the presence of common for both structures planar transition-metal built 6363 Kagome nets. Various stacking sequences of AB_5 and AB_2 result in the formation of three practically important stoichiometries, AB_3 ($1^*AB_5 + 2^*AB_2$), A_2B_7 ($1^*AB_5 + 1^*\ AB_2$) and A_5B_{19} ($3^*AB_5 + 2^*AB_2$). For each stoichiometry, either hexagonal ($2H$, $P6_3mc$) or rhombohedral ($3R$, R-$3m$) structures are formed depending on the stacking sequences. A–Mg–Ni compounds forming hydrides are widely studied due to their flexible chemistry and peculiar thermodynamic properties towards hydrogen uptake. They open the path to a rich chemistry with many new mixed compositions, allowing improved capacity uptake and corrosion resistance in alkaline medium. However, a deeper knowledge of their physicochemical properties, hydride formation paths and corrosion mechanisms are worth investigating to better understand their fundamental behavior.

As magnesium forms a Laves-type intermetallic compound $MgNi_2$, this compound can be used as a building block and when connected to the AB_5 block results in the formation of the AMg_2Ni_9 AB_3 intermetallic alloy, where two of the three rare-earth atoms are replaced by Mg atoms in an ordered way.

At the same time, when the relative amount of the AB_5 blocks increases, this limits Mg substitution in the AB_2 blocks to just 50% resulting in the formation of the $AMgNi_4$ slabs. Thus, magnesium content can broadly vary between ANi_3 and AMg_2Ni_9 for the AB_3 stoichiometry while it is limited to a maximum of A_3MgNi_{14} ($2^*ANi_5 + AMgNi_4$) for A_2B_7 stoichiometry with a similar limitation in maximum Mg content for the A_5B_{19} intermetallic ($3^*AB_5 + AMgB_4$) $-$ A_4MgNi_{19} [11].

This has important consequences as (a) magnesium is a light metal and decreases the density of the alloys resulting in a trend of increasing H density in the hydrides; (b) an atom of magnesium is much smaller compared to the atoms of the rare earth metals (Mg 1.60 Å vs La 1.877 Å), thus increasing the Mg content causes a contraction of the unit cells; (c) magnesium is subjected to a more active corrosion when in an alkaline electrolyte as compared to the rare earth; thus a surface layer of the alloys can be selectively leached affecting the performance of the anode electrodes. All these features should be properly accounted for when optimizing the type of the alloy and content of magnesium in this alloy.

When synthesizing the alloys in the required phase-structural composition, a fine-tuning of the annealing temperatures is required as shown by *in situ* studies of the transformations in the La–Mg–Ni AB_3 type alloys [14]. Theoretical studies using density functional theory (DFT) calculations were also performed for the AB_y phases and concluded on their structural stability in the (La,Mg)–Ni system [15]. In particular, DFT calculations showed that the energy difference between $2H$ and $3R$ polymorphic structures in superlattice alloys $(La,Mg)Ni_3$, $(La,Mg)_2Ni_7$, and $(La,Mg)_5Ni_{19}$ is very small and that compounds with half of the A site filled by Mg in the $[A_2B_4]$ sub-units are stable at 0 K.

Electrochemical behaviors—discharge capacity, high-rate discharge performance, cycling stability and calendar life—are very sensitive to changes in the magnesium content. Variations in Mg content in the $La_{3-x}Mg_xNi_9$ alloys affects such properties of the studied alloys as the phase homogeneity, hydrogen storage and electrochemical capacities, cycle stability, and high-rate discharge performance [16].

Mg substitution for La and annealing of the $La_{3-x}Mg_xNi_9$ alloys promotes the formation of more homogeneous materials, with a predominant formation of the target AB_3 $PuNi_3$ structure-type. The electrodes prepared from the annealed alloys show the maximum discharge capacity of $\sim$400 mAh g^{-1} (at $\sim$60 mA g^{-1}). The high-rate discharge-abilities at the discharge current density of 350 mA g^{-1} keep high values of the remaining reversible discharge capacities, $\sim$86, 85 and 80%, for the La_2MgNi_9, $La_{1.9}Mg_{1.1}Ni_9$ and $La_{1.8}Mg_{1.2}Ni_9$ alloy electrodes, respectively. After 200 cycles with 100% depth of discharge (DOD), the $La_{1.9}Mg_{1.1}Ni_9$ alloy electrode exhibits a very good cycling stability with 64% of its discharge capacity remaining. The most advanced performance is observed for the AB_3-type $La_{3-x}Mg_xNi_9$ alloys where 36.7% of La has been replaced with Mg as in the intermetallic alloy $La_{1.9}Mg_{1.1}Ni_9$. This performance can be related to the suitable stability of the hydride, allowing fast hydrogen exchange (figure 1(a)) and resulting is a high discharge capacity of mAh g^{-1} (figure 1(b)) and good performance at high discharge currents (figure 1(c)).

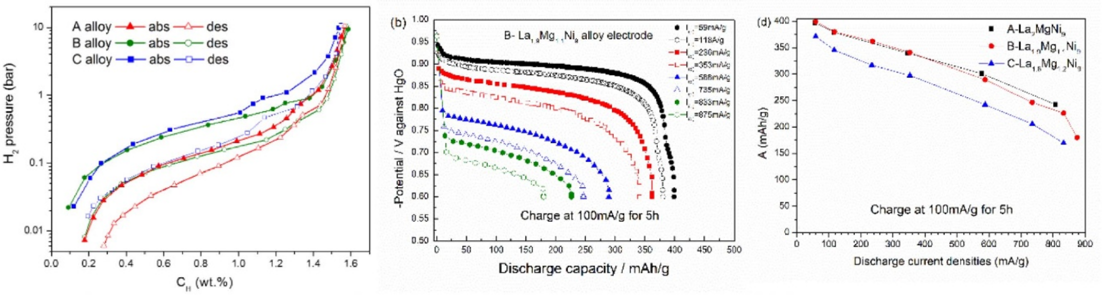

a **b** **c**

Figure 1. (a) P–C isotherms of hydrogen absorption-desorption at 293 K for the annealed La_2MgNi_9 (A), $La_{1.9}Mg_{1.1}Ni_9$ (B) and $La_{1.8}Mg_{1.2}Ni_9$ (C) alloys; (b) discharge curves of the electrodes in the relationship of discharge current densities, for the annealed $La_{1.9}Mg_{1.1}Ni_9$; (c) maximum discharge capacity versus applied current density. Reprinted from [16], Copyright (2021), with permission from Elsevier.

Operando neutron diffraction studies were applied to study the mechanism of transformations in the $LaNdMgNi_9$ AB_3 type anode. The electrochemical charge and discharge showed the formation of a saturated $LaNdMgNi_9D_{13}$ deuteride. Deuterium isotope was used instead of H to improve the quality of the data and to observe the sequence of transformations in the anode electrode during step-by-step electrochemical charge and discharge [17].

Reversible hydrogen storage and electrochemical capacity, thermodynamics of the metal-hydrogen interaction and corrosion resistance of the alloys and hydrides of the layered intermetallics are structure and composition dependent and it was established for the A_2B_7 intermetallic alloys containing La, Gd, Sm, Y and Mg in [18, 19]. For rare-earth substituting alloys $A_{2-x}La_xNi_7$ (A = Y, Gd, Sm), multi-plateau Pressure-Composition-Isotherms are obtained with maximal capacity ranging from 9 to 11 H/f.u. In contrast, La by Mg substitution leads to a single plateau pressure and reversible interaction. Interestingly, the combination of rare-earth and Mg substitutions results in improved sorption properties within the thermodynamic window suitable for electrochemical applications: 0.001–0.1 MPa at room temperature. Thus, a reversible capacity equivalent to 400 mAh g^{-1} is anticipated for the compound $La_{1.1}Sm_{0.5}Mg_{0.4}Ni_7$.

2.2. Rare earth-free materials

Laves type AB_2 intermetallics are a focus of the electrochemical studies since they are rare earth-free metal hydride anodes. This is the most abundant group of intermetallic compounds containing ~1000 binary and ternary compounds. Three types of Laves type structures have the most representatives, hexagonal C14, FCC C15 and hexagonal C36 types.

For the Laves-type AB_2 intermetallic compounds, rare earth metals, zirconium, titanium, calcium, and magnesium are the main elements on the A sites. A variety of elements used on the B sites most frequently includes such elements as aluminum, vanadium, chromium, manganese, iron, cobalt, nickel, and copper. Formation of multicomponent Laves phase compositions containing a mixture of the components on both A and B sites proved to be efficient in achieving advanced hydrogenation-dehydrogenation performance particularly when applied as the metal hydride anode electrodes of the Ni-MH batteries. The compositional and structural disorder is introduced to the MH materials on three different length scales using elemental composition and processing techniques of alloys and electrodes. The length scales over which disorder is created can be designated as (a) atomic, which comprises regions with dimensions up to a few nearest-neighbor atomic distances; (b) intermediate-range, regions from 10 to 20 nm extending up to ~100 nm; and (c) long-range, with regions exceeding 100 nm. Disorder on each of these length scales is used to achieve different performance parameters of the hydrogen storage alloys.

Atomic size factor and electron concentration are two main factors affecting both formation of the Laves type intermetallics and a particular type of the structure—C14 or C15—but also their hydrogenation properties and electrochemical performance as anodes of the metal hydride batteries [20].

One particular type of alloys has great flexibility in chemical composition and is described by the formula $(Zr_{1-x}Ti_x)(Ni, Mn, V, Fe)_{2\pm y}La_{0.01-0.05}$ ($x = 0.15$–0.22; $y = 0.05$–0.10). Various aspects of metal-hydrogen interactions in such alloys were studied by Yartys *et al* in a series of publications [21–27]. The multielement composition $Ti_{0.15}Zr_{0.85}La_{0.03}Ni_{1.126}Mn_{0.657}V_{0.113}Fe_{0.113}$ was selected based on the in-house research performed at IFE, Norway of the $AB_{2\pm x}$ C15 Laves-type alloys for their application as hydrogen storage and battery electrode materials. In multi-element $AB_{2\pm x}$ alloys, constituting elements contribute to the H storage performance in a variable way. Indeed, Ti, Zr and V are the hydride forming elements, Ni has a high catalytic activity, Co and Mn provide surface activity relevant for hydrogen exchange, and Cr, Al and Fe increase alloy stability. One typical composition is $Ti_{0.15}Zr_{0.85}La_{0.03}Ni_{1.126}Mn_{0.657}V_{0.113}Fe_{0.113}$. Please, note that the alloy contains small additions of La for the improvement of the activation performance and cycling stability.

Variation of the stoichiometry in the $C15$ type AB_2 based alloys and their microstructural modification by application of the rapid solidification technique plays an important role in designing these alloys as it has a significant effect on the phase structural and electrochemical properties allowing to achieve improved performance [21–27]. The stoichiometry was changed in these studies in two ways; (a) change in the Zr/Ti ratio; and (b) variation of the B/A ratio between under stoichiometric $AB_{1.90}$ and over stoichiometric $AB_{2.077}$. A slightly under stoichiometric $AB_{1.95}$ alloy (with x in AB_{2-x} 0.05; $Zr + Ti + La = 1.03$; $Ni + Mn + V + Fe = 2.009$; $B/A = 2.009/1.03 = 1.95$) showed excellent hydrogen sorption properties (high reversible storage capacity, easy activation, fast kinetics and low hysteresis of isotherms of hydrogen absorption-desorption). This suggested that it could be very promising for both storage of hydrogen gas and also for the electrochemical application as anode in the metal hydride batteries. La forms a secondary LaNi intermetallic compound which acts as a catalyst for the hydrogenation of the AB_2 alloy (figure 2).

2.3. Mg-rich anodes

Hydrides of Mg-based alloys have high electrochemical discharge capacity (theoretical limit reaches 999 mAh g^{-1} for Mg_2NiH_4) and abundant resources, and therefore, are promising anode materials for Ni-MH batteries [28]. However, they suffer from a very serious capacity decay in charge/discharge cycling, which has been attributed to the corrosion of Mg in alkali electrolyte. Numerous studies have been conducted to solve this problem in the past decades, and the most common method is the partial substitution of Ni and Mg by other elements such as Zr, Cr, Ti, Al, Co, Y, Pd and Pt [29, 30]. For example, the capacity retention for $Mg_{0.8}Ti_{0.1}Pd_{0.1}Ni$ alloy is 200 mAh g^{-1} after 80 cycles. Improvements by chemical substitution remain unfortunately rather limited.

Recently, studies of the capacity fading of the milled Mg-Ni based alloy electrodes have revealed the origin of the observed capacity loss by comparing the behaviors of the crystalline Mg_2Ni, nanocrystalline Mg_2Ni and amorphous $Mg_{0.5}Ni_{0.5}$ alloys [31]. It has been found that it is the amorphous MgNi phase that contributes to achieving the reversibility of the electrochemical capacity. Then, it was also confirmed that the hydrogen-induced crystallization (HIC) during the hydrogenation process is the dominant reason for the capacity decay in the milled Mg-Ni anode alloy, further to its electrochemical corrosion. By comparing the electrochemical properties of $Mg_{0.50}Ni_{0.50}$, $Mg_{0.45}Ti_{0.05}Ni_{0.50}$ and $Mg_{0.40}Ti_{0.10}Ni_{0.50}$ alloys together with their microstructural evolution during cycling [32], it was demonstrated that Ti addition suppresses the HIC in the amorphous Mg-Ni, and thus improves the cyclic performance of the alloy electrodes. This clearly proves that Ti addition does not substantially improve the corrosion resistance of the alloy electrodes, thus the governing mechanism of the transformations suggested in the previous studies appears to be different from the presently observed behaviors. The milled $Mg_{0.40}Ti_{0.10}Ni_{0.50}$ can achieve an initial capacity of 425 mAh g^{-1} and maintains 55.7% of this capacity after 30 cycles, while the milled $Mg_{0.50}Ni_{0.50}$ only maintains 24% of its initial capacity of 515 mAh g^{-1}.

Owing to the corrosion, however, the milled Mg-Ni alloy shows a certain capacity decay, even though Ti addition enhances the stability of its amorphous phase. To address this problem, 4.5 M tetramethylammonium hydroxide (TMAH) was selected as a new electrolyte [33]. It was found that the discharge capacity of $Mg_{0.40}Ti_{0.10}Ni_{0.50}$ electrode in this electrolyte is 210 mAh g^{-1} after 100 cycles, much higher than that in 6 M KOH electrolyte (69 mAh g^{-1}). Moreover, with the addition of $Cu(OH)_2$ to the 4.5 M TMAH electrolyte, Cu becomes electrodeposited on the surface of $Mg_{0.4}Ti_{0.1}Ni_{0.5}$ alloy electrode during the charging process and because of this further improves its cyclic stability and also increases its electrochemical reaction rate. The $Mg_{0.40}Ti_{0.10}Ni_{0.50}$ electrode retains ∼74% of its initial discharge capacity in 4.5 M TMAH + 0.01 M $Cu(OH)_2$ electrolyte after 100 cycles. Figure 3 summarizes the above results.

2.4. Improved MH battery cells and the hydride battery for large scale endurable electric grid solutions

The performance of cylindrical cells made from negative electrode active materials of two selected AB_2 metal hydride chemistries with different dominating Laves phases (C14 vs. C15) were compared. Cells made from C15 alloy showed a higher high-rate performance and peak power with a corresponding sacrifice in capacity, low-temperature performance, charge retention, and cycle life when compared with the C14 counterpart (alloy C14) [34].

Development of the metal hydride batteries progresses further at a company Nilar with their Headquarters in Stockholm, Sweden. Nilar continues to approach the market with new, innovative nickel-metal-hydride-based energy storage solutions. Today's developments include:

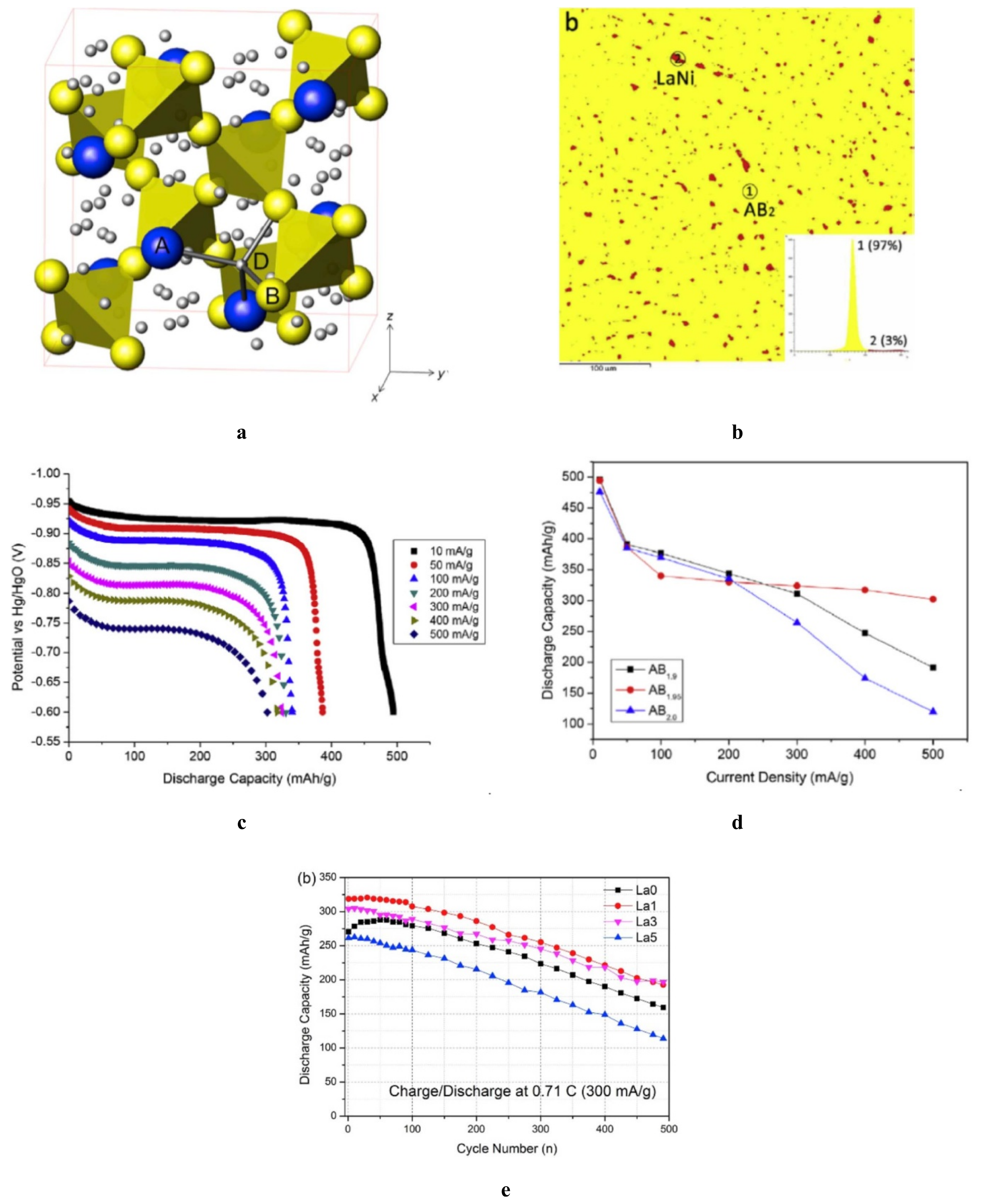

Figure 2. Properties of the $C15$ Laves type $(Zr_{1-x}Ti_x)(Ni, Mn, V, Fe)_{2\pm y}La_{0.01-0.05}$ ($x = 0.15$–0.22; $y = 0.05$–0.10) intermetallic compounds: (a) the alloy forms a hydride containing 3–4 at. H/f.u. with hydrogen atoms exclusively occupying $(Zr,Ti)_2B_2$ interstitial tetrahedral sites as is shown by the neutron powder diffraction study. Reprinted from [23], Copyright (2019), with permission from Elsevier. (b) Catalyzing effect of small additions of La is related to the formation of finely dispersed LaNi intermetallic alloy as La is not dissolved in the AB_2 (Zr,Ti-based Laves type alloy. LaNi actively forms a hydride $LaNiH_{3.7}$ which catalyses the hydrogenation of the Laves type intermetallic. Reprinted from [21], Copyright (2019), with permission from Elsevier. (c) Discharge capacity is the highest between the similar alloys reaching 495 mAh g^{-1}. Reprinted from [26], Copyright (2020), with permission from Elsevier. (d) The alloys show excellent performance at high discharge current densities. Reprinted from [26], Copyright (2020), with permission from Elsevier. (e) The best cycling stability of the $Ti_{0.2}Zr_{0.8}La_{0-0.05}Ni_{1.2}Mn_{0.7}V_{0.12}Fe_{0.12}$ alloy is obtained for 3 wt.% (La3) with a capacity retention of 63% after 500 cycles. Reprinted from [23], Copyright (2019), with permission from Elsevier.

- Large increase in production volume.
- Standardization of product range.
- Expand sales reach to all corners of the world.

From an overall user perspective, long battery cycle is important to bring down the overall cost and life impact of a battery system. Much focus is on battery capacity, but for rechargeable batteries, rechargeability is

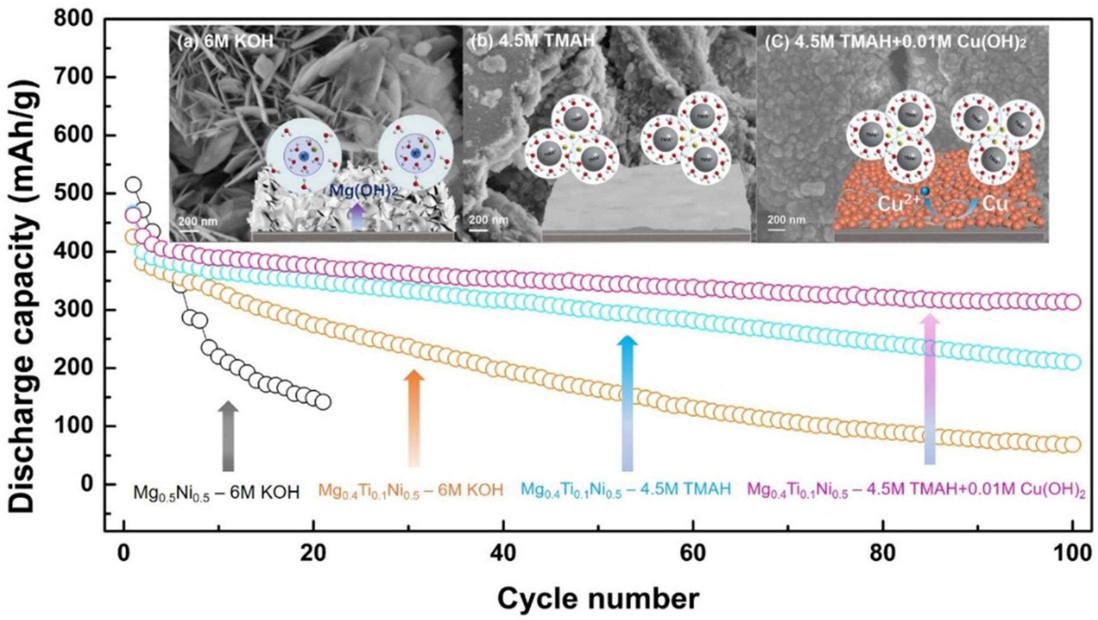

Figure 3. The cyclic stability of the milled $Mg_{0.40}Ti_{0.10}Ni_{0.50}$ and $Mg_{0.5}Ni_{0.5}$ alloys used as anode electrodes in various electrolytes. $Mg_{0.4}Ti_{0.1}Ni_{0.5}$ when studied in 4.5 M TMAH with addition of 0.01 M $Cu(OH)_2$ shows a clearly superior performance.

more relevant, i.e. the total energy throughput during the battery lifetime: Throughput = Cycle life × Capacity.

Increasing the cycle life of the NiMH battery can make it the preferred choice for energy storage in electric grid applications. It is especially important to support the electrical grid as more intermittent solar and wind power stations are connected.

Recent development utilizing gas-phase reactions in the battery casing has made it possible to significantly increase the cycle life [35]. In 2015, a patent application regarding adding oxidants to an aged NiMH battery was filled by Nilar International AB, based on collaborative research with Stockholm University [36].

The inspiration to the development came from the nickel-hydrogen battery (NiH_2), which has an extremely long cycle life which has promoted its used in space applications. The NiH_2 battery is a good choice for long-lasting space missions, especially in low orbit missions where the number of cycles becomes significant. NiH_2 batteries have orbited the earth as well as Mercury (Messenger) and Mars (Odyssey and Global Survivor). When the NiH_2 batteries in the Hubble Space Telescope were replaced after 19 years, they had reached the highest number of charge/discharge cycles ever. But using gaseous hydrogen means a relatively low volumetric efficiency. The NiMH battery has a significantly higher volumetric efficiency, almost on par with several of the common Li-battery chemistries. The high volumetric efficiency is a consequence of the high volumetric hydrogen storage density in solid-state metal hydrides, which supersedes that of liquefied hydrogen. The hydride battery has until now not been able to reach the long cycle life of the NiH_2 battery as the metal hydride undergoes slow corrosion that consumes the electrolyte, which in turn dries up the battery. In addition, the corrosion also evolves hydrogen gas that is absorbed in the metal hydride leading to an imbalance of the charge states of the electrodes with respect to each other. This can lead to increased internal battery pressure and a premature venting of the safety seal, accelerating the drying out of the battery. The amount of corroded alloy is, however, only a few percent of the total content in the battery cells, when the end-of-life is reached caused by the electrolyte dry-out [37, 38]. By adding oxygen and hydrogen to the internal battery casing, the electrolyte can be refilled and the imbalance of the electrodes can be corrected. The expected amount of alloy corroded can also be compensated for in the initial design of the battery cells. This will make it possible to increase the total energy throughput beyond that of corresponding Li-battery chemistries where the corrosion products are insolvable lithium-containing oxides. The corrosion product of the charge carrier (H) in the hydride battery is water molecules, which anyhow is the solvent of the electrolyte.

The simplicity of the hydride battery chemistry is also an advantage compared to storing the energy as hydrogen gas, since hydrogen has to be electrolyzed from water, compressed or liquefied to be stored and then supplied to a fuel cell to get the electricity back. The overall energy efficiency of this chain is low. A

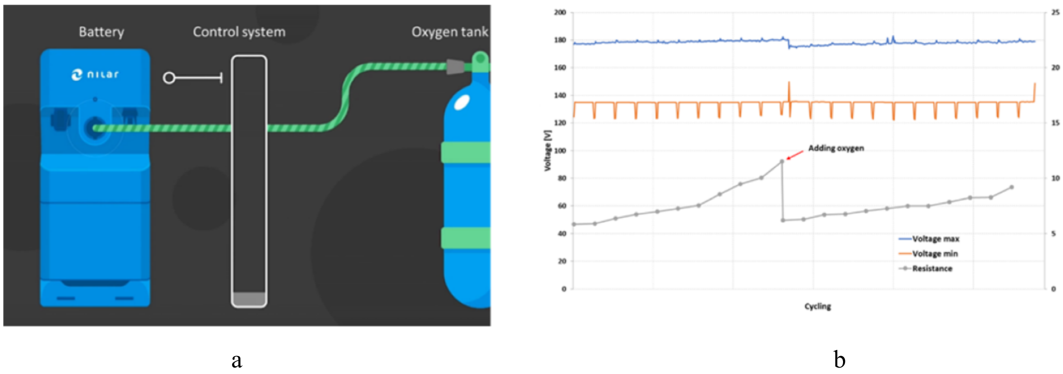

Figure 4. (a) Schematic drawing of the automated gas filling system which has been developed to restore aged 144-volt NiMH battery packs; (b) maximum and minimum voltages during 0.5 C cycling of a 144-volt battery pack. The spikes in the cycling curves correspond to measurements of the total pack capacity and internal resistivity.

battery solution is technically simpler with the benefit of an increased overall efficiency compared to an electrolyzer/fuel cell solution.

Nilar now has a new battery design with a gas refill fixture connected to an oxygen gas tank (figure 4(a)), and the gas filling process is performed by an automated control system. A safe region for a refill has been defined in terms of a voltage threshold and maximum aging level. The present battery system is based on 12 modules with each 10 bipolar NiMH cells all in a common gas space, to which gases can be added. So, all in all 120 cells are filled at the same time. In the future, larger systems, with more cells will be offered. Due to legislative issues concerning safety, only oxygen additions will be used at present. This will still multiply the cycle life of the battery pack and the system. Figure 4(b) shows an improved performance data based on the use of the proposed design solution. In the longer term also hydrogen addition will be included allowing the battery packs and systems to aim for a similar long cycle life as NiH_2 batteries.

3. High-capacity MH anodes for Li-ion (or Na-ion) batteries using conversion reaction

Metal hydrides are attractive anodes for Li-ion batteries thanks to their high specific and volumetric capacities along with their low potential [12]. They have been tested in combination with both classical liquid electrolytes [39, 40] and novel solid electrolytes for the next generation of SSBs [41–43]. Li-metal is the ultimate anode of Li-ion ASSBs but this choice is highly challenging due to severe volume changes of the anode, electrochemical reduction of certain electrolytes at the low Li^+/Li potential (e.g. sulfides) and formation of short-circutting dendrites. Despite the fact that metal hydrides have a lower specific capacity than Li metal, their use as a host can undoubtedly help to mitigate some of these issues.

Among all suitable metal hydrides (figure 5), only a few of them have been recently reported as effective anode materials of LIB. In this section, two families are considered: (a) magnesium-based and (b) 3*d* metal-based materials.

3.1. Mg-based alloys

Magnesium hydride is the most studied hydride compound as a conversion type anode for Li-ion batteries. Its ability to react electrochemically with lithium, according to the conversion reaction $MgH_2 + 2Li^+ + 2e^- \leftrightarrow Mg + 2LiH$, was demonstrated in the pioneering work of Oumellal *et al* [46]. Gravimetric and volumetric capacities associated with this reaction are 2036 mAh g^{-1} and 2880 mAh cm^{-3}, respectively. The equilibrium potential is $E_{eq} = 0.55$ V vs. Li^+/Li as derived from the Nernst law and the enthalpy of formation of magnesium and lithium hydrides [47].

Despite the favorable thermodynamic properties of MgH_2, its use as an anode in LIB encounters two major challenges: a large volume change of 85%, and the incomplete reversibility of the conversion reaction at room temperature. These two issues have been highlighted by Berti *et al* [48] on a fundamental electrochemical study using 1 μm thick MgH_2 thin film as a 2D model system in a standard liquid electrolyte. Combined galvanostatic potential profiles and transmission electron microscopy (TEM) analysis (figure 6) evidenced that, during lithiation, the conversion progresses as a front reaction from the top to the bottom of the thin film, which doubles its thickness after full conversion. On de-lithiation, no reaction front is observed, and the reversibility is limited to 25%. As determined from TEM analysis and electrochemical impedance spectroscopy (EIS) measurements, this low reversibility was assigned to slow reaction kinetics within the film at room temperature and not to mechanical degradation or electronic insulation issues. This

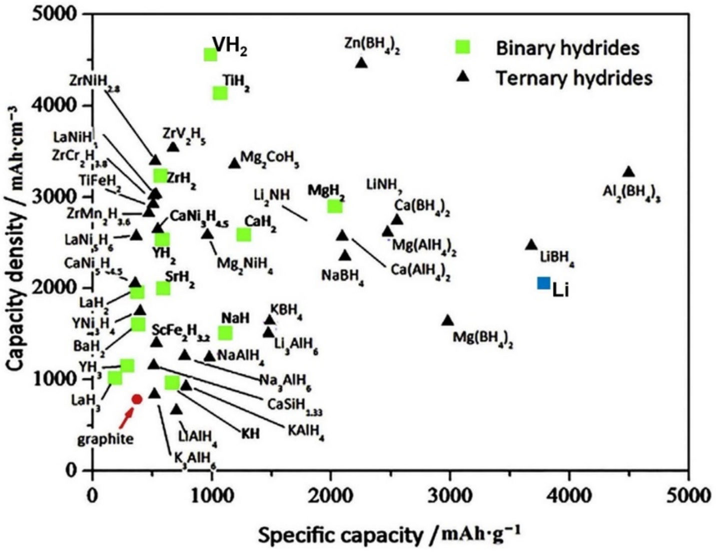

Figure 5. Mass and volume capacities for different metallic hydrides based on the conversion reaction with lithium following the chemical reaction: $M\mathrm{H}_x + x\mathrm{Li} \leftrightarrow M + x\mathrm{LiH}$ and the density of the hydrides. Reprinted from [44], Copyright (2018), with permission from Elsevier.

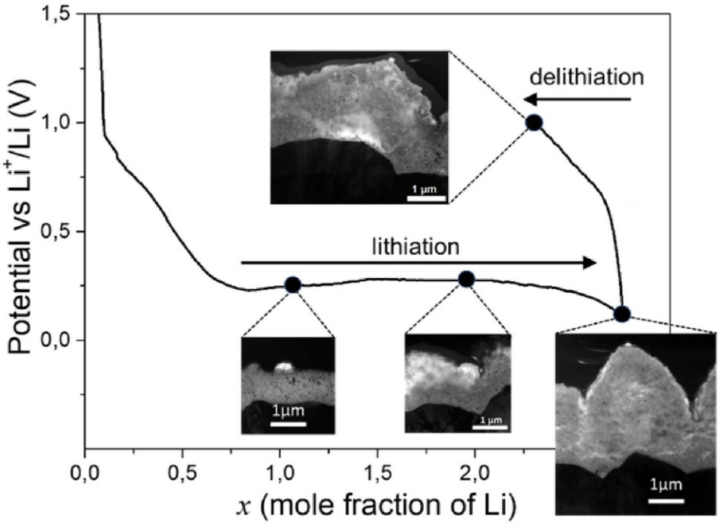

Figure 6. Galvanostatic potential profiles at room temperature and TEM bright field images of the conversion reaction between lithium and 1 μm $\mathrm{MgH_2}$ film at a cycling rate of C/50. Lithiation is observed at 0.3 V vs $\mathrm{Li^+/Li}$ for mole fraction of lithium, x, in the range $0.75 < x < 2.75$, and is preceded by Solid Electrolyte Interface (SEI) formation for $x < 0.75$. Formation of LiH crystals is evidenced by white areas in TEM images. De-lithiation for a cut-off potential of 1 V vs $\mathrm{Li^+/Li}$ occurs within the range $2.25 < x < 2.75$.

conclusion concurs with EIS studies on 3D composite-type porous electrodes prepared from ball-milled $\mathrm{MgH_2}$ slurries [49].

Sluggish kinetics of the conversion reaction with $\mathrm{MgH_2}$ have been surmounted in solid-state half-cells using $\mathrm{LiBH_4}$ as superionic electrolyte by increasing cell temperature to 120 °C [43, 50]. This temperature is mandatory to achieve high ionic conductivity for the borohydride. Besides the temperature effect, it was suggested and later confirmed [51] that $\mathrm{LiBH_4/MgH_2}$ interfaces within the composite anode favor H-transport within the negative electrode. The addition of vapor-grown carbon nanofibers to enhance the electrical conductivity allowed cycling rates up to 4 C for a reversible capacity of 1200 mAh $\mathrm{g^{-1}}$.

High reversibility and capacity have also been achieved on complex hydride $\mathrm{Mg_2FeH_6}$ used as anode operating at 120 °C. Huen and Ravnsbæk showed that the conversion reversibility could be enhanced by a factor of three on cycling the $\mathrm{Mg_2FeH_6}$ anode in solid-state half-cells as compared to the conventional liquid-electrolyte [52]. Interestingly, $\mathrm{MgH_2}$ was proposed to be formed as an intermediate during the conversion reaction.

3.2. 3*d* metals and other systems

To keep the largest energy densities, research has been focused on light 3*d* metal hydrides, mostly TiH_2 and VH_2. Titanium hydride was first reported as a conversion material by Oumellal *et al* [53, 54] and later implemented in a solid-state half-cell by Kawahito [55] using $LiBH_4$ as a solid electrolyte. This material exhibits good reversible behavior at 120 °C, producing 1052 mAh g^{-1} with a capacity retention of 83% for 50 cycles at $C/4$ (400 mA g^{-1}).

Nanocomposites MgH_2-TiH_2 are remarkable materials due to synergetic effects between the two hydride constituents both in solid-gas [56] and electrochemical [57, 58] reactions. Dao *et al* demonstrated that there is a compositional trade-off between MgH_2 and TiH_2 constituents for electrochemical applications. The former hydride provides a higher specific capacity and the latter ensures better cycling stability [41, 59]. This work paved the way to the proof of concept of a hydride-based ASSB using hydride compounds both for the negative electrode ($0.8MgH_2$–$0.2TiH_2$) and the solid electrolyte ($LiBH_4$) [60]. Such a battery was completed using Li_2S at the cathode. It worked at 120 °C and delivered 780 mAh g^{-1} for 25 cycles at various rates ($C/10$ to $C/50$) with a Coulombic efficiency (CE) of 97%.

Recently, Matsumura *et al* [61] reported the properties of VH_2, a well-known hydride for hydrogen storage with high volume capacity. As the dihydride is unstable at atmospheric pressure and room temperature, the authors started from a mixture of V and LiH instead of the hydride. A half-cell using Li as counter-electrode and $LiBH_4$ as solid electrolyte was built and cycled at 125 °C. Analysis of the electrochemical curves and x-ray diffraction at different potential allow identifying different processes i.e. expected conversion reactions between VH_y ($y = 0.8$ and 2) and Li but also a significant contribution from lithiated carbon formed during the ball milling of the composite electrode (a mixture of $V + LiH + LiBH_4 +$ acetylene black). In addition, the dihydride VH_2, unstable at the operating temperature, spontaneously desorbed gaseous hydrogen upon charging. Finally, the reversible capacities remain in the range between 400 and 200 mAh g^{-1} for a few cycles.

It can be anticipated that further research on metal hydrides as conversion anodes will consider novel battery chemistries beyond the Li-ion technology based on alternative cations such as Na, Mg and Ca. So far, only the Na case has been somewhat explored. Xu and Mulder reported the conversion between MgH_2 and Na at room temperature, but the reaction extent and the underlying mechanism could not be clearly established [62]. Also, the potential relevance of lithium-aluminum amide $LiAl(NH_2)_4$ as the Na anode has been proposed based on first-principles calculations [63]. Further works on metal hydrides for Na-ion and multivalent batteries will certainly attract a lot of interest.

4. Monovalent superionic conductor complex hydrides as electrolytes for advanced Li/Na batteries

4.1. Basic concept of superionic conductivity of complex hydrides, mainly on $BH_4{}^-$ and $NH_2{}^-$ based materials

All-SSBs that employ solid-state electrolytes are among the most prominent candidates to resolve the intrinsic drawbacks of conventional liquid-based lithium-ion batteries, such as electrolyte leakage, flammability, and limited energy density. Ionic-conducting solid electrolytes are the key component of all-SSBs because their ionic conductivity and chemical/electrochemical stability determine the battery's performance. Complex hydrides, generally denoted as $M_x(M_y{}'H_z)$ (where M represents a metal cation and $M_y{}'H_z$ represents a complex anion), have recently received particular attention as promising solid electrolyte systems for all-SSBs, because of the high ionic conductivity of their high-temperature (high-T) phases [64–67]. A common characteristic of complex hydrides is a significant rise in the ionic conductivity by the phase transition accompanied by their structural change from an ordered low-temperature (low-T) phase to a disordered high-T phase. On the basis of this phenomenon, initial interest in complex hydride ionic conductors has mainly focused on lithium borohydride ($LiBH_4$) and related derivative materials. $LiBH_4$ undergoes a structural phase transition to the high-T hexagonal phase at ~390 K, accompanied by a substantial increase in conductivity. The high-T phase of $LiBH_4$ is known to have dynamical disorder of the $[BH_4]^-$ anions which lead to generate of a Li^+ metastable state located at an interstitial site [68]. The rotational disorder of the BH_4 units have been evaluated by synchrotron x-ray powder diffraction and quasi-elastic neutron scattering (QENS), in addition to *ab initio* molecular dynamics simulations [69–72]. After the given phase transition, the high-T phase of $LiBH_4$ exhibits a lithium ion conductivity of $>10^{-3}$ S cm^{-1}, which is three orders of magnitude higher than that of its low-T phase [65–67].

On the basis of DFT calculations, Li-ion migration has been analyzed by means of the nudged elastic band method for the $LiBH_4$, Li_2NH, $Li_2BH_4NH_2$, $Li_4BH_4(NH_2)_3$, and $Li_5(BH_4)_3NH$ structures [73]. Additionally, a statistical analysis has been performed for most conductive and studied complex hydrides, i.e. $LiBH_4$, Li_2NH, $Li_2BH_4NH_2$, $Li_4BH_4(NH_2)_3$, and $Li_5(BH_4)_3NH$, to obtain the average values for the

Table 1. Structure and space groups (SG), average values of Li-ionic conductivity at 30 °C, activation energy (E_A) and ln σ_0 obtained by the statistical analysis performed for the different investigated complex hydrides. Data taken from [73].

Compound	Structure (SG)	Li-ion conductivity at 30 °C (S cm^{-1})		E_A (eV)		ln σ_0	
$LiBH_4$	Orthorhombic(*Pnma*)	9.5×10^{-9}	$\pm 2.07 \times 10^{-9}$	0.75	±0.07	16	±2
$LiNH_2$	Tetragonal($I\bar{4}$)	5.36×10^{-11}	$\pm 4.11 \times 10^{-11}$	0.98	±0.06	19	±2
Li_2NH	Cubic($Fm\bar{3}m$)	3.66×10^{-4}	$\pm 8.92 \times 10^{-5}$	0.60	±0.04	21	±2
$Li_2NH_2BH_4$	Trigonal ($R\bar{3}$)	1.01×10^{-4}	$\pm 1.63 \times 10^{-5}$	0.69	±0.06	23	±2
$Li_4(NH_2)_3BH_4$	Cubic ($I2_13$)	1.54×10^{-4}	$\pm 4.09 \times 10^{-5}$	0.37	±0.02	10.1	±0.6
$Li_5(BH_4)_3NH$	Orthorhombic (*Pnma*)	1.29×10^{-7}	$\pm 8.33 \times 10^{-8}$	0.73	±0.03	18	±2

activation energy, lnσ_0 and Li-ion conductivity at 30 °C (see table 1). Although no clear correlation between static topological properties (e.g. crystal structure and channel sizes) and Li-ion conductivity of Li–B–N–H compounds could be found, the combination of the calculated defect formation and migration energy is in good agreement with the experimental activation energies values, suggesting that the topological analysis can be used to explain the Li-ion conductivity in the studied compounds.

Halide substitution is one of the approaches to enhance the room temperature Li^+ conductivity in $LiBH_4$, by stabilizing the hexagonal polymorph at this temperature. To this end, The $LiBH_4$-LiBr phase diagram has been explored experimentally by means of powder diffraction (PXD), *in situ* synchrotron radiation (SR)-PXD, and differential scanning calorimetry (DSC), and thermodynamically assessed using the calculation of phase diagrams (CALPHAD) method coupled with *ab initio* results [74]. The hexagonal h-$Li(BH_4)_{1-\alpha}(Br)_\alpha$ solid solution was found stable in the range $0.30 \leqslant \alpha \leqslant 0.55$ at room temperature and a peritectic reaction at 380 °C ($\alpha = 0.60$) was observed [74]. By combining DSC and PXD analyses, an enthalpy of mixing ($\Delta H_{\mathrm{Mix}} = 1.0 \pm 0.2$ kJ mol^{-1}) for the formation of the h-$Li(BH_4)_{0.6}(Br)_{0.4}$ solid solution has been obtained from the CALPHAD assessment. For the first time, a ternary hexagonal solid solution, h-$Li(BH_4)_{1-\alpha-\beta}(Br)_\alpha(Cl)_\beta$, containing chloride and bromide was stabilized at room temperature, lowering the weight of the electrolyte, and thereby increasing the energy density [75].

The above-mentioned approach reliess on the formation of a solid solution via anion substitution, which can often stabilize the disordered high temperature polymorph structure to lower temperatures than for the pure material. However, high dynamics of BH_4^- complexes in the solid-state can also occur in materials with ordered structures such as for the series of new compounds, $LiRE(BH_4)_3Cl$, RE = La, Ce, Pr, Nd, Gd, Sm [76–80]. Despite the ordered anion lattice, there is a significant disorder in the distribution of Li^+ occupying 2/3 of the available positions. These structural properties may explain the very high Li^+ ion conductivity, e.g. $\sigma(Li^+) = 1.03 \times 10^{-4}$ S cm^{-1} for $LiCe(BH_4)_3Cl$ at $T = 20$ °C. DFT calculations suggest that this structure type is stabilized by higher entropy rather than lower energy [77, 78, 80]. The Li-ion diffusion was measured by pulsed-field-gradient (PFG) NMR at 400 K for $LiLa(BH_4)_3Cl$ and was found to exceed 10^{-7} cm^2 s^{-1} [80]. Within the series $LiLa(BH_4)_3X$, X = Cl, Br, I, the bromide substituted variant has the highest Li^+ conductivity $\sigma(Li^+) = 7.74 \times 10^{-5}$ S cm^{-1} at room temperature and 1.8×10^{-3} S cm^{-1} at 140 °C [81]. Based on structural analysis using powder x-ray diffraction data and DFT calculations, a new cation conductivity pathway was found. Empty sites which can accommodate interstitial lithium ions are connected by triangular openings spanned by three anions, denoted as bottleneck windows. Hence, the bromide analogue has the optimal 'window' sizes allowing for the fastest Li^+ migration in contrast to the Cl and I analogues, which have less ideal 'windows' [81].

In addition to ion substitution, various other approaches have been explored for improving the ionic conductivity of $LiBH_4$-based compounds; effective approaches reported recently include using thin films [82], and reactive mixtures leading to new conductive phases (e.g. $LiBH_4$–NH_3 systems), nanoconfinement [83] and so on.

$LiBH_4 \cdot {}^1\!/_2 NH_3$ (hemiammine lithium borohydride), is a new type of fast Li^+ ionic conductor, $\sigma(Li^+) = 7 \times 10^{-4}$ S cm^{-1} at 40 °C in the solid-state [84]. The structure is layered in the *a*–*c* plane built from $[Li(BH_4)_4]$ and $[Li(BH_4)_3NH_3]$ tetrahedra, which are stacked along the *b*-axis and interconnected by short dihydrogen bonds, 2.03–2.07 Å, B–$H^{\delta-} \cdots {}^{+\delta}H$–N. The Li^+ migration pathway of $LiBH_4 \cdot {}^1\!/_2 NH_3$ was investigated in detail by DFT. During Li^+ migration, NH_3 is exchanged between interstitial and framework Li^+, while the BH_4^- reorients to stabilize the coordination of lithium ions. The energy landscape of an interstitial Li^+ moving through the unit cell in the *a*–*c* plane is characterized by two maxima of ~0.16 eV, which may be rate-determining for the conductivity. The first maximum is associated with the exchange of a BH_4^- ligand, while the second maximum is associated with the exchange of an NH_3 ligand. After a step forward of the interstitial Li^+–NH_3 complex, the NH_3 molecule is delivered back to the initial framework Li^+, and the migration only involves a modest displacement of framework Li^+ and nitrogen of up to ~1.1 and ~0.7 Å, respectively. The coordination of the Li^+ is reasonable for all metastable and intermediate configurations during the migration pathway [84]. Thus, the fast *ligand-assisted* lithium conductivity is due to a new *general* cation conductivity mechanism similar to the one discussed in detail for $Mg(BH_4)_2{\cdot}NH_3$ later in this review (chapter 5) and denoted *pas-de-deux*. This cation conductivity mechanism occurs due to a very flexible structure owing to di-hydrogen bond networks, and the flexible coordination of the BH_4^- complexes.

4.2. Nanoconfined and composite materials

Increased ion mobility of $LiBH_4$ based composites which are melt-infiltrated into for example, mesoporous SiO_2 scaffolds [83], has been known for a while. As the interface between $LiBH_4$ and SiO_2 is largely responsible for the increased ion mobility, the ionic conductivity of $LiBH_4$ can also be enhanced, simply via mixing with nonporous SiO_2 nanoparticles [85]. To study the origin of the improved ionic conductivity in complex hydride/metal oxide composites, a detailed dynamic model for $LiBH_4$-SiO_2 composites have been formulated using solid-state NMR measurements at various temperatures [86]. The influence of oxide surface groups on the Li-ion conductivity of $LiBH_4$–SiO_2 composites was also investigated by systematically varying the density and nature of the SiO_2 (Santa Barbara Amorphous (SBA)-15) surface groups. The results show clearly that the density of the free surface silanol groups strongly affects the composite Li-ion conductivity, suggesting that the interaction between $LiBH_4$ and the silica surface groups is crucial to the enhanced ionic conductivity [87].

Composites of $LiBH_4$ and Al_2O_3 exhibited high ionic conductivity of 2×10^{-4} S cm^{-1} at room temperature when the volume fraction of Al_2O_3 was ∼44% [88]. This increase in ionic conductivity was attributed to the formation of a highly defective interface between $LiBH_4$ and Al_2O_3, as manifested by B–O bonds detected by the near edge x-ray absorption fine structure measurements. A first-principles study on the defect structure and the Li ion migration in orthorhombic-$LiBH_4$ proposed that the much lower Li ion conductivity of orthorhombic-$LiBH_4$ compared to hexagonal $LiBH_4$ is due to higher defect formation energy rather than due to lower mobility [89]. Therefore, an increased defect concentration at the interface, i.e. higher number of charge carriers, may significantly enhance ionic condution.

The effect of adding various nanosized oxides (i.e. SiO_2, CaO, MgO, γ-Al_2O_3, TiO_2, and ZrO_2) by ball-milling on the Li-ion conductivity of $LiBH_4$, has recently been reported, showing an enhancement of the RT Li-ion conductivity in all the composites [90]. Subsequently, following these guidelines, $LiBH_4$-MgO composites have been optimized in terms of compositions, reaching a Li-ion conductivity of 2.86×10^{-4} S cm^{-1} at 20 °C [91].

In an effort to further boost the room temperature ionic conductivities in complex hydrides, the two main approaches of conductivity enhancement, i.e. anion substitution and nanoconfinement, were successfully combined [92–94]. The studies were carried out to exploit the possible synergistic effects of the two methods. To this end, anion substituted $LiBH_4$ ($Li(BH_4)_{1-x}(I)_x$ and $Li_2(BH_4)_{1-x}(NH_2)_x$) have been confined in nanoporous SiO_2 or Al_2O_3. The ionic conductivity of the nanocomposites of $LiBH_4$–LiI–Al_2O_3 reached 1.0×10^{-4} S cm^{-1} at room temperature [93] figure 7. It has been reported that the conductor-insulator nano effects are independent of the choice of the bulk crystal structure of $LiBH_4$, either being orthorhombic ($LiBH_4/Al_2O_3$) or hexagonal ($LiBH_4$–LiI/Al_2O_3). At the same time, the LiI-stabilized layer-structured form of $LiBH_4$ guarantees fast two-dimensional (2D) bulk ion dynamics and contributes to facilitating fast, long-range ion transport [92]. Results on $LiBH_4$–$LiNH_2$ confined in mesoporous silica (mobil composition of matter (MCM)-41) show that this concept is also applicable to other Li-bearing hydrides, reaching an RT Li-ion conductivity of 5.0×10^{-4} S cm^{-1} [93]. In this system, the enhanced conductivity has been attributed to the stabilization of a highly conductive phase inside the scaffold pores, rather than the formation of a conductive interfacial layer at the oxide/hydride interface as observed for nanoconfined $LiBH_4$ [95].

Likewise, the compound, $LiBH_4{\cdot}{}^1\!/_2NH_3$, has a low melting point associated with a significant increase of conductivity, $\sigma(Li^+) = 3.0 \times 10^{-2}$ S cm^{-1} at 55 °C. The molten state of $LiBH_4{\cdot}{}^1\!/_2NH_3$, has a high viscosity and can be mechanically stabilized in nano-composites with inert metal oxides, making it a promising battery electrolyte [84, 98].

Solvated $Li_2B_{12}H_{12} - x$Solv. (Solv. = acetonitrile or tetrahydrofuran) showed unexpected melting at low temperature (<150 °C), which improved the conductivity to 0.08 mS cm^{-1}. As acetonitrile-based electrolytes have shown remarkable stability towards lithium-based anodes [100, 101], these results provide new research avenues worth considering. The melting feature was utilized to melt infiltrate $Li_2B_{12}H_{12}$ into a mesoporous silica SBA-15 scaffold. However, the desired improvement of ionic conductivity was limited and instead, a slight increase in diffusion activation energy was observed from 0.52 eV for pristine $Li_2B_{12}H_{12}$ to 0.60 eV for the $Li_2B_{12}H_{12}$-SBA15 sample [102].

In addition to oxides, sulfides has also been used for composite electrolytes. The ball-milled composite 0.9 (3 $LiBH_4$ + LiCl) + 0.1 P_2S_5 contained a LiCl-like phase with broad diffraction peaks and somewhat

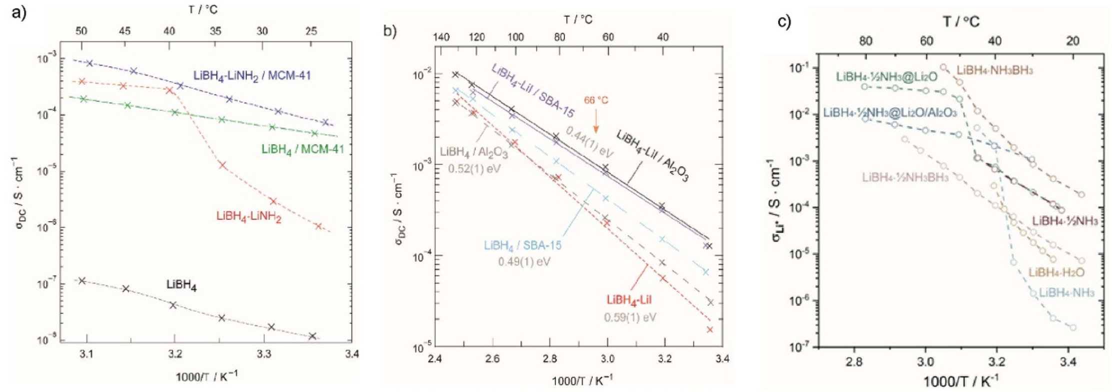

Figure 7. Combined effects of ion substitution and nanoconfinement on the ionic conductivity of $LiBH_4$: (a) $LiBH_4$-$LiNH_2$/SiO_2 nanocomposites, (b) $LiBH_4$-LiI nanoconfined in SiO_2 and Al_2O_3. Reprinted with permission from [93]. Copyright (2020) American Chemical Society. (c) Temperature-dependent Li-ion conductivity of selected $LiBH_4$ complexes with neutral ligands. ($LiBH_4 \cdot H_2O$ [96]. $LiBH_4 \cdot NH_3$ [97]. $LiBH_4 \cdot {}^1/_2NH_3$ [84, 98]. $LiBH_4 \cdot {}^1/_2NH_3$@Li_2O/Al_2O_3(60 wt%) [98]. $LiBH_4 \cdot xNH_3BH_3$ [99]).

Table 2. The approaches to enhance the Li ion conductivity of $LiBH_4$.

Approach	Material	Li-ion conductivity at 25 °C (S cm^{-1})	Reference
—	$LiBH_4$	$\sim 10^{-8}$	[65, 73]
Halide substitution (High-T phase stabilization)	$3LiBH_4$–LiI	$\sim 10^{-5}$	[65–67]
Cation substitution	$LiCe(BH_4)_3Cl$	$\sim 10^{-4}$	[76–80]
Neutral ligands	$LiBH_4$–NH_3BH_3	$\sim 10^{-4}$	[99]
Oxide composite	$LiBH_4$–Al_2O_3	$\sim 10^{-4}$	[83, 88, 90]
Sulfide composite	$0.9(3LiBH_4 + LiCl) + 0.1\ P_2S_5$	$\sim 10^{-5}$	[103]

larger unit cell than LiCl, which was interpreted as a $LiCl_{1-y}(BH_4)_y$ with y estimated to be 0.4 from Vegard's law. Bragg peaks from $LiBH_4$ had almost disappeared, and there was pronounced diffuse scattering indicating the formation of an amorphous phase [103]. The Li-ion conductivity (σ) of the as-milled composite was relatively poor (10^{-5} S cm^{-1} at RT). Upon heating, the conductivity first increases rather slowly, but from about 75 °C it increases more sharply. The conductivity remained high upon cooling and was in the range of 10^{-3} S cm^{-1} at near-ambient temperature. A second heating/cooling run resulted in a σ vs $1/T$ curve which followed the first cooling curve rather closely. *In-situ* SR-PXD revealed that the sharp increase in conductivity upon the first heating coincides with a complete and irreversible amorphization of the material. Composites with higher P_2S_5 contents were mostly or completely amorphous after milling and did not exhibit any transition to a highly conductive state upon heating. The approaches and the resulting Li ion conductivities of the representative $LiBH_4$-related materials are summarized in table 2.

4.3. (Car)borane based materials

In an effort to improve the properties of complex hydrides, primarily the ionic conductivity, a series of *closo*-(car)boranes containing *closo*-type (cage-like) complex anions, such as $[CB_9H_{10}]^-$, $[CB_{11}H_{12}]^-$, and $[B_{12}H_{12}]_{2-}$, have been intensively investigated [66, 104–106]. *Clos*o-(car)boranes contain not only multiple H atoms but also multiple B and C atoms. This atomic environment leads to unique covalent bonding patterns (boron–boron, boron–carbon, boron–hydrogen, and/or carbon–hydrogen), which gives rise to large cage-like polyanionic structures. Therefore, compared to $LiBH_4$-based hydrides, *closo*-(car)boranes intrinsically have the advantage of higher ionic conduction, because of large diffusion channels and low electrostatic interaction between the lithium ions and complex anions, both of which are mainly attributed to the large sizes of *closo*-type complex anions ($[B_{12}H_{12}]^{2-}$: 5.8 Å vs $[BH_4]^-$: 2.0 Å). Indeed, the high-*T* phases of *closo*-(car)boranes exhibit high ionic conductivities of $\sim 10^{-1}$ S cm^{-1}, which is two orders of magnitude higher than that of $LiBH_4$.

Among the numerous *closo*-(car)boranes studied thus far, the high-*T* phase (space group *P*31*c*) of $Li(CB_9H_{10})$ has been studied most extensively as a solid electrolyte because of its low phase-transition temperature (90 °C) and high lithium-ion conductivity (8.1×10^{-2} S cm^{-1} at 110 °C) [105].
In particular, partial substitution of $[CB_9H_{10}]^-$ in $Li(CB_9H_{10})$ with other complex anions such as $[CB_{11}H_{12}]^-$ and $[B_{12}H_{12}]^{2-}$ (i.e. $(1-x)Li(CB_9H_{10}) - xLi(CB_{11}H_{12})$ system [107, 108] and

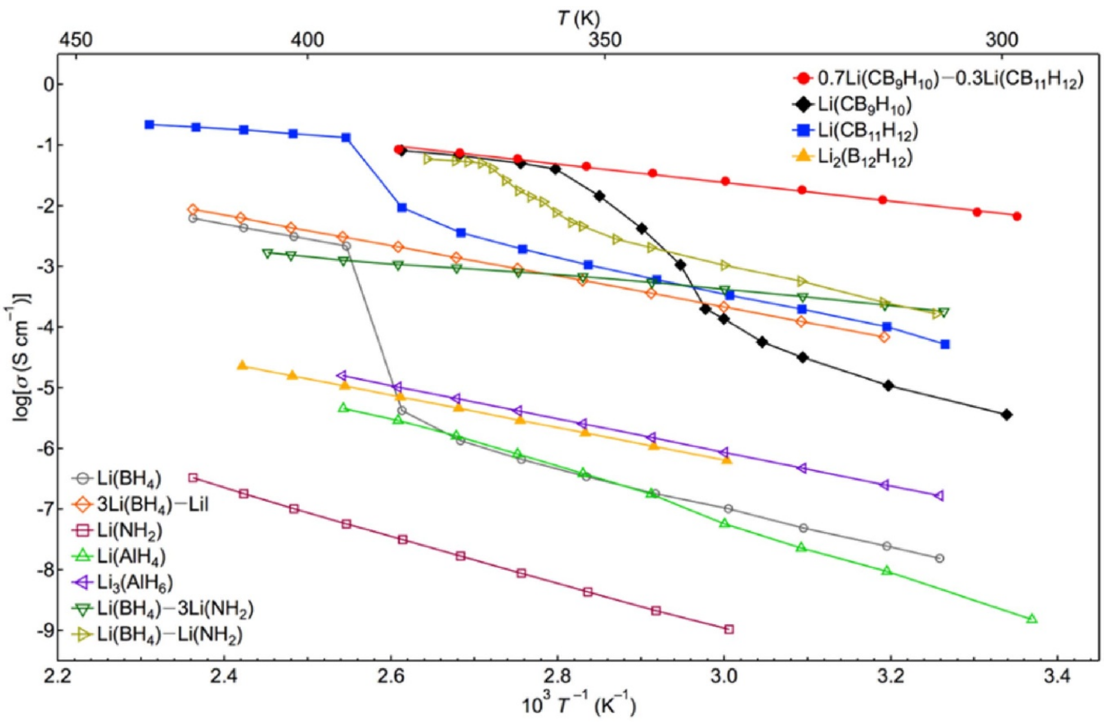

Figure 8. Ionic conductivities of various complex hydrides. Reproduced from [108]. CC BY 4.0.

$(1-y)\mathrm{Li(CB_9H_{10})}-y\mathrm{Li_2(B_{12}H_{12})}$ system [109] enables a disordered hexagonal framework consistent with that of the high-T phase of $\mathrm{Li(CB_9H_{10})}$ (hexagonal unit cell with the space group $P31c$) to be obtained at room temperature. Importantly, the stabilized high-T phases exhibit lithium superionic conductivities of $>10^{-3}$ S cm^{-1} at 25 °C. Among them, $0.7\mathrm{Li(CB_9H_{10})}$–$0.3\mathrm{(CB_{11}H_{12})}$ showed the highest ionic conductivity (figure 8). Its ionic conductivity at room temperature and activation energies (E_a) were 6.7×10^{-3} S cm^{-1} and 28.4 kJ mol^{-1}, respectively [108]. This conductivity is comparable to those of oxide-based and sulfide-based solid electrolytes. Considering that organic liquid electrolytes have transport numbers of below 0.5, $0.7\mathrm{Li(CB_9H_{10})}$–$0.3\mathrm{(CB_{11}H_{12})}$ has higher conductivity than organic liquid electrolytes.

The per-halogenated sodium-*closo*-dodecaborates, $\mathrm{Na_2B_{12}Cl_{12}}$, $\mathrm{Na_2B_{12}Br_{12}}$, and $\mathrm{Na_2B_{12}I_{12}}$ compounds are isostructural, and undergo order–disorder polymorphic transition at increasing temperatures, 475 °C, 525 °C, and 570 °C, respectively. This is much higher compared to the parent compound $\mathrm{Na_2B_{12}H_{12}}$ (266 °C), and their $\mathrm{Na^+}$ conductivity are also significantly lower [110, 111]. Intra-molecular anion substitution with iodine in lithium *closo*-borates has also been investigated. For the deca-borates, mono-, di-, and persubstituted within iodine, $\mathrm{Li_2[B_{10}H_9\text{-}1\text{-}I]}$, $\mathrm{Li_2[B_{10}H_8\text{-}1,10\text{-}I2]}$, and $\mathrm{Li_2B_{10}I_{10}}$, leads to about one-order of magnitude higher $\mathrm{Li^+}$ conductivity as compared to the parent compound, $\mathrm{Li_2B_{10}H_{10}}$, in the temperature range of 25 °C–300 °C [112].

The series of $M_2\mathrm{B_{12}(OH)_{12}}$, M = Li, Na, K, and Cs compounds, reveal that the ionic conductivities depend on the cation size of the alkali metal and is highest for $\mathrm{Li^+}$, 5.97×10^{-5} S cm^{-1}, and lowest for $\mathrm{Cs^+}$, 1.60×10^{-8} at 250 °C. The relatively low conductivities compared to similar $M_2\mathrm{B_{12}H_{12}}$ compounds may be due to the higher mass of the anion, the lower degree of dynamics in the anion lattice, or stronger and directional anion–cation interactions [113]. Ammine sodium decahydro-*closo*-decaborane, $\mathrm{Na_2B_{10}H_{10}}\cdot x\mathrm{NH_3}$, $x = 1$ or 2, was investigated, but revealed low $\mathrm{Na^+}$ conductivity of $\sigma(\mathrm{Na^+}) = 2 \times 10^{-8}$–$5 \times 10^{-8}$ S cm^{-1} at ambient temperatures. These values are significantly lower compared to the parent compound, $\mathrm{Na_2B_{10}H_{10}}$, and are assigned to an anchoring effect of ammonia limiting or preventing anion dynamics [114].

The carborate anion, e.g. $[\mathrm{CB_{11}H_{12}}]^-$, has lower charge-density (q/V) as compared to the parent *closo*-borates, e.g. $[\mathrm{B_{12}H_{12}}]^{2-}$, from where they originate by substitution of one boron atom for a carbon. The most well-known and stable members of this class of interesting materials are $[\mathrm{HCB_9H_9}]^-$ and $[\mathrm{HCB_{11}H_{11}}]^-$. Cation mobility and polymorphic transitions are often closely related to interactions and disorder in the anion lattice. Eleven polymorphs of $M(\mathrm{HCB_{11}H_5}X_6)$ (M = Li or Na, X = Cl or Br) are identified and structurally investigated [115]. They have order–disorder polymorphic transitions in the temperature range 203 °C–305 °C and show $\mathrm{Li^+}$ and $\mathrm{Na^+}$ superionic conductivities in the disordered states of 6–35 mS cm^{-1}. Fast cation mobility is assigned to asymmetric polarizability of the *closo*-carborate anions due to substitution with halogen atoms, the anion reorientational mobility and the lattice symmetry [115].

Lately, also the open-caged *nido*-borate $[B_{11}H_{14}]^-$ anion has attracted interest. $LiB_{11}H_{14}$ and $NaB_{11}H_{14}$ have been investigated and in combination with anion substitution, e.g. $[B_{12}H_{12}]^{2-}$, $[CB_9H_{10}]^-$, and $[CB_{11}H_{12}]^{2-}$ anions resulting in a range of compounds, e.g. $Na_4(B_{11}H_{14})_2(B_{12}H_{12})$ and $Li_2(B_{11}H_{14})(CB_{11}H_{12})$ [116]. Recently, $KB_{11}H_{14}$ was added to the series, whereas the hydrated version of $LiB_{11}H_{14}\cdot(H_2O)_n$ and $NaB_{11}H_{14}\cdot(H_2O)_n$ were found to have high ionic conductivities with the latter reaching 1.1×10^{-3} S cm^{-1} [117, 118]. Finally, $Li_2(B_{11}H_{14})(CB_{11}H_{12})$ was employed as an electrolyte in a half cell with TiS_2 as the cathode, which showed an 82% capacity retention up to 150 cycles at C/5 ending at ∼150 mAh g^{-1} [119].

4.4. Computational approach for superionic conductivity of complex hydrides

One of the most promising emerging classes of complex hydride-based superionic conductors is based on salts of anionic polyboron nanocages ($M_2B_{12}H_{12}$, $M_2B_{11}H_{11}$, $M_2B_{10}H_{10}$, $MCB_{11}H_{12}$, MCB_9H_{10}, $MB_{11}H_{14}$, M = Li, Na). Many of these variants display exceptional ionic conductivities, driven by the formation of a phase with rotationally disordered anion configurations [105, 111, 115, 116, 118, 120–130]. Beyond high ionic conductivity, polyborates have a number of additional advantages over more conventional solid electrolytes. They are extremely lightweight and pliable, allowing for easy processing. They also feature a large palette of potentially tunable chemistries, which can be further modified by partial or total substitution of H with halogen atoms (F, Cl, I). They also have high electrochemical stability windows [131]. Nevertheless, one of the limitations is the range of thermal stability of the superionic phase, which typically activates at elevated temperatures in most variants. An active area of research internationally is the extension of the superionic phase to room temperature, generally by mixing select *closo*-(car)borate electrolyte compositions [118, 121, 132–135]. A few of these variants have also been recently incorporated into demonstration battery designs [118, 132–134].

Alongside the experimental activities, a number of computational and joint investigations have significantly improved the understanding of the underlying motivations for superionic conductivity in these materials [111, 115, 120, 136–140]. Wood *et al* performed a series of computational 'experiments' and detailed analyses based on *ab initio* molecular dynamics of parent compounds $Li_2B_{12}H_{12}$ and $Na_2B_{12}H_{12}$ to identify three governing factors, deemed by the authors as chemical, structural, and dynamical frustration [111]. Here, frustration refers to a flattening of the energy landscape due to competing physicochemical preferences that prevent the formation of deep local minima for cation migration. Similar analyses were recently extended to carbon- and halogen-decorated *closo*-borates [115, 120], as well as $M_2B_{10}H_{10}$ compounds [141]. The three classes of frustration were expanded and refined in a recent perspective paper, which discusses superionic motivations for *closo*-borates in the broader context of other solid electrolytes [141].

One subclass of chemical frustration refers to a conflict between local anion geometry, which templates the short-ranged interaction with nearby cations, and the lattice packing, which dictates the longer-ranged electrostatic cation packing. In superionic *closo*-borates phases, crystallographic rearrangement leads to a highly entropic state in which these two factors are fundamentally irreconcilable [111, 141]. Chemical frustration can also arise from a perturbation of the charge density on the anion itself upon substitution of carbon for boron in carboborates or by partial halogenation [115, 120]. This creates an intrinsic dipole that further disrupts the electrostatic symmetry of the anion. Halogenation with larger anions further enhances local polarizability, which changes the nature of the short-ranged interaction and can lead to new enhancements in ionic conduction, as shown in a recent joint experiment-theory study by Jørgensen *et al* [115].

Structural frustration is associated with the lattice itself, including how lattice geometry affects site preferences for cation occupation [111, 140, 141]. The computational studies of Wood *et al* found that superionic phases of these materials do not feature strong preference for a particular variety of interstitial site (tetrahedral/trigonal/linear) [111, 141]. They also found that superionic *closo*-borates experience large fluctuations in local coordination environments [111, 140, 141]. This unusual lack of site preference and presence of local off-stoichiometry leads to a large number of effectively available vacant sites, which the authors captured in a calculation of Shannon configurational entropy [111, 141]. Nevertheless, the authors' survey of computed activation barriers across a wide variety of *closo*-borates variants found no significant correlation between crystal structure and ion mobility, which confirms that anion packing is not the only governing factor [140].

Dynamical frustration refers to the onset of anion rotation above the superionic transition temperature, which creates a dynamically shifting energy landscape that helps to prevent cation ordering while simultaneously transferring momentum to aid conduction [111, 141]. A number of studies have confirmed the connection between anion rotation and ion mobility in *closo*-borates [124, 129]. The study by Dmitrievska *et al* combined experimental QENS with *ab initio* molecular dynamics and QENS computations to reveal the complex reorientational dynamics of $LiCB_{11}H_{12}$ and $NaCB_{11}H_{12}$ [120]. They found that the introduction of carbon on the complex anion introduces anisotropy into the anion reorientations, which works synergistically with the intrinsic anion dipole to further corrugate the energy landscape dynamically. These corrugations are much more energetically significant than for the carbon-free $Li_2B_{12}H_{12}$ and $Na_2B_{12}H_{12}$, which may explain their higher low-temperature ionic conductivity.

These abovementioned studies are largely based on DFT within the generalized gradient approximation, typically using the *ab initio* molecular dynamics scheme. This method is highly accurate, making it useful for probing detailed mechanisms. However, the computational expense limits the system sizes and simulation durations that can be easily studied. To address this issue, a few recent studies have reported the development and application of classical interatomic potentials that can access larger-scale phenomena in closo-borate salts, including phase transitions and better resolved transport coefficients [138, 139]. These investigations can operate hand-in-hand with the *ab initio* studies to guide future experimental approaches towards optimizing the superionic phase transition and the accompanying ionic conductivity.

4.5. Experimental characterization for superionic conductivity of complex hydrides

In order to understand the ion conduction mechanisms in the complex metal hydrides, it is necessary to characterize the compounds with techniques that can probe local dynamics such as QENS and solid-state NMR. These techniques have previously demonstrated their significance by the exploration of the paddle-wheel mechanism [135, 142] and are incredibly strong tools for investigating the hydrogen jump rates in hydrogen-rich materials such as hydroborates. Recent studies on MCB_9H_{10} and $M_2B_{10}H_{10}$ ($M =$ Li, Na) show that the reorientational jump rate of the $CB_9H_{10}{}^-$ anion increases by almost two orders of magnitude during the transition from the ordered low-temperature phase to the disordered high-temperature phase [143]. Additionally, $NaCB_9H_{10}$ displays jump frequencies 60% to 120% higher than $LiCB_9H_{10}$ and $Na_2B_{10}H_{10}$, which correlates well with the liquid-like ionic conductivity of $NaCB_9H_{10}$ of 0.03 S cm^{-1} even at room temperature [105, 143]. Investigations on $MCB_{11}H_{12}$ ($M =$ Li, Na) also show that the introduction of carbon in the boron cage modifies the orientational preferences of the anions and aids the rotational mobility. In combination with a significant change in the cation-anion interaction, these effects facilitate the high ionic conductivity [126].

Recent PFG spin-echo NMR experiments emphasize the fast Li^+ diffusivities in complex metal hydrides. Specifically, at 400 K the measured diffusion coefficient for $LiCB_9H_{10}$ exceeds 10^{-6} cm^2 s^{-1}. Similarly, the measured diffusion coefficients for the complex hydrides $Li_3(NH_2)_2I$ and $LiLa(BH_4)_3Cl$ exceed 5×10^{-8} cm^2 s^{-1} and 10^{-7} cm^2 s^{-1} [81]. The family of bimetallic borohydrides-halides $LiLa(BH_4)_3X$ ($X =$ Cl, Br, I) exhibit high ionic conductivities. All the compounds exhibit very fast reorientational motion of the $BH_4{}^-$ groups, determined from the proton spin-lattice relaxation rates [80, 144]. Interestingly, the reorientational process becomes faster with the increasing radius of the halide ion. Additionally, ^{7}Li NMR results support higher Li^+ diffusivity with both increasing reorientational motion of the $BH_4{}^-$ groups and increasing halide ion radius, which is also consistent with the ionic conductivities of the compounds [80, 144, 145].

Another thoroughly studied approach to improving the ionic conductivity of $LiBH_4$ based compounds is to create composites with insulating materials. One example is a 30/70 wt% $LiBH_4/SiO_2$ aerogel, which has an ionic conductivity of 0.1 mS cm^{-1} at room temperature. QENS and NMR studies indicate the presence of two different $LiBH_4$ fractions with different Li and H mobilities—one fraction with high mobilities that account for the high ionic conductivity, and one fraction accounting for macrocrystalline $LiBH_4$ with lower mobility. Ultimately, the interaction between $LiBH_4$ and the SiO_2 surface facilitates a high ionic conductivity. In the present composition, a fraction of 10% of the ions have a high mobility, determined from NMR. In order to improve this type of system, the contact area between $LiBH_4$ and SiO_2 should be maximized while staying within the percolation threshold [146]. Similar effects are seen in both $LiBH_4$ with various nanosized oxides and nanoconfined $LiBH_4$–LiI/Al_2O_3 [90, 94], as well as MBH_4-C_{60} ($M =$ Li, Na) nanocomposites [147].

5. Novel fast cationic electrolytes, towards new battery concepts

5.1. Liquid and ionic liquid boron-hydrogen based electrolytes

Batteries based on multivalent cations and metallic anodes such as Mg, Ca, and Al have been attracting increased interest due to the high natural abundance of these metals, their benign nature compared to Li and Na metals, and relatively high theoretical battery energy density. The R&D in these areas has been particularly hampered by the propensity of these metals to readily passivate when put in contact with most

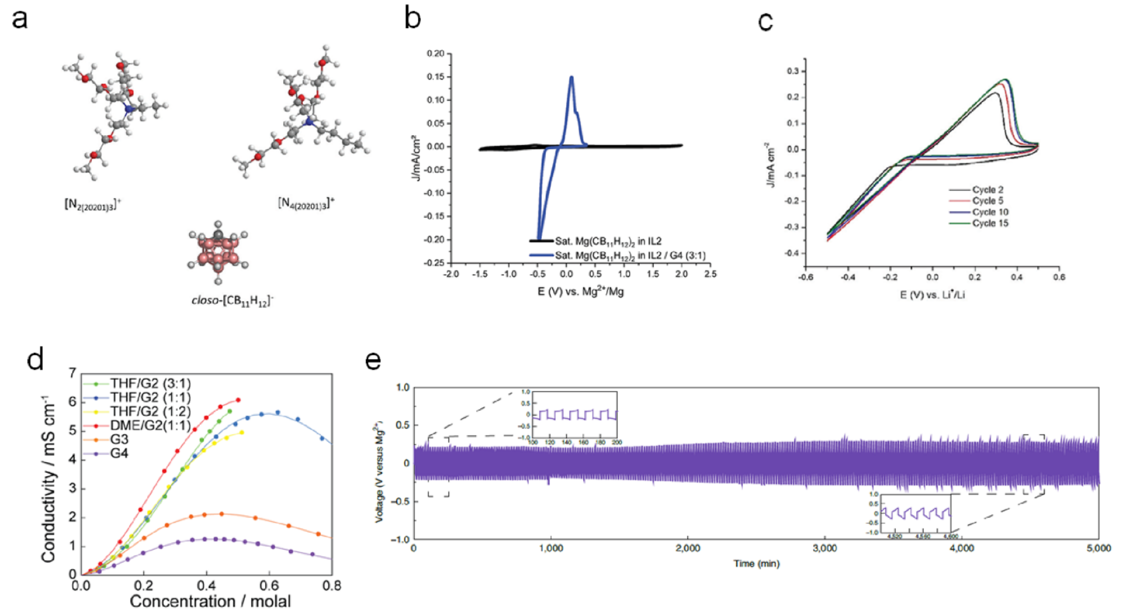

Figure 9. (a) Structures of $[N_{2(20201)3}]$ $[CB_{11}H_{12}]$ (IL1) and $[N_{4(20201)3}][CB_{11}H_{12}]$ (IL2). ($N_{2(20201)3}$: N-ethyl-N,N,N-tris(2-(2-methoxyethoxy)ethyl)ammonium cation, $N_{4(20201)3}$: N-butyl-N,N,N-tris(2-(2-methoxyethoxy)ethyl) ammonium cation, blue, O = red, C = grey, H = white, B = pink). (b) Cyclic voltammogram CV on Pt electrode of a saturated $Mg[CB_{11}H_{12}]_2$ solution in IL2 (black) (cycle 10) and in IL2/G4 (3:1) (cycle 10). (c) CV of 0.2 M $Li[NTf_2]$, NTf_2: bis(trifluoromethanosulfonyl) imide, in IL2 over 15 cycles under inert conditions. (RE: Li, CE: Li, WE: Ni) at 60 °C. (d) Ionic conductivity dependence on the concentration of MMC solutions in selected glymes and ethereal solvent mixtures at 25 °C. (e) Galvanostatic voltage profiles of a Mg|Mg symmetric cell cycled for plating/stripping 3 mAh cm^{-2} per cycle at a current density of 20 mA cm^{-2}. (a)–(c) Reproduced from [151] with permission from the Royal Society of Chemistry. (d), (e) Reproduced from [152], with permission from Springer Nature.

non-aqueous electrolytes [148]. In an effort to overcome this critical issue, designs of boron-hydrogen based electrolytes have proven effective in enabling highly efficient metal plating and stripping and supporting the battery function, as explained next. It is expected that this class of electrolytes can provide improved safety and power in new types of SSBs.

High compatibility of boron-hydrogen salts with a multivalent metal was first reported by Mohtadi *et al* [149], and was achieved through designs based on $Mg(BH_4)_2$ in ethereal solutions for a Mg battery. Given the measured low anodic stability of the BH_4^- anion (1.7 V vs. Mg/Mg^{2+}) and guided by computational studies, the same research group expanded the electrochemical stability window by exploiting the 3D aromaticity of the B–H bonds in *closo*-borates. In particular, the *closo*-monocarborate $Mg(CB_{11}H_{12})_2$ (MMC) electrolytes exhibited high stability (4.9 V vs. Mg/Mg^{2+}) [150] exceeding that of the ethereal solvents and were subject of recent studies that utilized the stability of the *closo*-monocarborate anion to design ionic liquid solvents as alternatives for ethers [151]. Ionic liquids have also been investigated as potentially safer electrolytes due to their low flammability, negligible vapor pressure, and high thermal stability. The key for the success of this study was lowering the glass transition temperature, T_g (i.e. melting), of the ionic liquids to below −30 °C so that they are appropriate for battery applications. This was achieved by design of ammonium cations that incorporated long and flexible alkoxy side chains (figure 9(a)) used to compensate for the structural rigidity of the cluster, which tends to promote elevated melting points. The ionic liquids prepared had glass transition temperatures as low as −52 °C and supported efficient Li and Mg metal plating and stripping (figures 9(b) and (c)). They also offered about 0.5 V gain in the anodic stability vs. that obtained in ethers and had good ionic conductivities in the order of 10^{-4} S cm^{-1} at 30 °C.

One highly desired property of an electrolyte is fast bulk and interfacial cationic conductivity that enables fast battery discharge and charge rates. This was recently reported for a Mg metal battery that utilized modified MMC ethereal electrolytes [152]. Limitations of ionic transport kinetics in these electrolytes were attributed to the high binding energy and viscous nature of the triglyme (G3) and tetraglyme (G4) solvents, the only ethereal solvents found capable of dissolving the MMC salt. Discovery of the solubility of MMC in ethereal mixtures alleviated this challenge and prompted the designs of optimized electrolyte solutions. In particular, the MMC solution in monoglyme/diglyme (DME/G2) substantially improved the bulk transport (figure 9(d)), ∼6 times increase in room temperature conductivity vs. that in tetraglyme. Facile kinetics of the Mg anode was observed and manifested in high CE, wherein a 99.7% was achieved at rates as high as 50 mA cm^{-2} (figure 9(e)). Importantly, the morphology of Mg deposited on Cu substrate at currents as high as 20 mA cm^{-2} (areal capacity of 3 mAh cm^{-2}) were dense and dendrite-free, while smooth voltage profiles in symmetric Mg|Mg cell cycling under the same conditions demonstrated effective mass transport. A Mg metal battery prototype incorporating this electrolyte and an organic pyrene-4,5,9,10-tetraone cathode demonstrated high specific power capabilities of 30.4 kW kg^{-1}, which is close to two orders of magnitude higher than the current state-of-the-art Mg battery (0.45 kW kg^{-1}) [152].

5.2. Tetrahydridoborate-based solid-state divalent cationic electrolytes

Solid-state inorganic divalent cationic conductors with useful conductivity ($\sigma(M^{2+}) > 10^{-4}$ S cm^{-1}) at ambient temperatures have until recently been limited to solution and polymer-based electrolytes. However, the extreme expansion of metal borohydride materials and derivatives has revealed new types of electrolytes. Chapter four of this review reveals that a complex metal hydride, $LiBH_4 \cdot ½NH_3$, exhibits a new conductivity mechanism for monovalent cations. Here, we further discuss this mechanism, denoted *pas-de-deux*, and argue that it is general for both mono- and divalent cations and possibly also for a range of other related compounds.

Magnesium borohydride, $Mg(BH_4)_2$, is known to have a very low Mg^{2+} conductivity and almost behaves as an insulator. However, when magnesium is complexed by a neutral molecule, the Mg^{2+} conductivity may increase by several orders of magnitude, initially illustrated using a bidentate ligand, ethylene diamine (*en*), forming $Mg(BH_4)_2 \cdot NH_2(CH_2)_2NH_2$ with a high conductivity of $\sigma(Mg^{2+}) \sim 6 \times 10^{-5}$ S cm^{-1} at $T = 70$ °C, and negligible electronic conductivity, which is a prerequisite for a successful electrolyte, see figure 10 [153]. Recently, a series of compounds, $Mg(BH_4)_2 \cdot xNH_3$, $x = 1, 2, 3$, and 6 were also found to have very high Mg^{2+} conductivity, e.g. $\sigma(Mg^{2+}) \sim 3.3 \times 10^{-4}$ S cm^{-1} at $T = 80$ °C observed for $Mg(BH_4)_2 \cdot NH_3$ [154].

The crystal structure of the new compound $Mg(BH_4)_2 \cdot NH_3$ is orthorhombic and it is built from zig-zag chains of—BH_4–Mg–BH_4–Mg—along the *b*-axis with one terminal (κ^3) and two bridging (κ^2) BH_4^- groups. The chains are interconnected by dihydrogen bonds, B–$H^{\delta-} \cdots {}^{+\delta}$H–N, between the terminal BH_4^- and the NH_3 groups, with either relatively strong (∼1.80 Å) or weaker (∼2.25 Å) bonds. The mechanism for cation migration was investigated in detail using DFT by calculating the energy profile of an interstitial Mg^{2+} migrating along the *b*-axis throughout the unit cell [154]. The largest energy barriers ($E_a \sim 1$ eV) are associated with the transfer of a neutral NH_3 molecule from a lattice magnesium to the interstitial Mg^{2+} and back again to the same lattice Mg^{2+} after a translation of the migrating ion. The transfer of NH_3 occurs via molecular rotation and displacement or via an 'umbrella'-type molecular inversion. The DFT structural analysis reveals a high degree of structural flexibility and stability since only the interstitial Mg^{2+} is translated in the solid-state whereas lattice Mg^{2+}, NH_3, and BH_4^- are only displaced forth and back relative to their crystallographic positions. The impressive structural flexibility of $Mg(BH_4)_2 \cdot NH_3$ is associated to a varying and changing coordination of the BH_4^- (κ^1, κ^2, or κ^3) ligand, and the extended di-hydrogen bond network, which stabilizes the intermediate positions. Lattice magnesium are displaced up to 2.68 Å, but the coordination of both lattice and interstitial Mg is almost ideal for all DFT optimized intermediates and metastable positions with a Mg coordination number ∼8. Notice, that di-hydrogen bonds in the solid-state resemble hydrogen bonds in the biological matter and have similar bond lengths of ∼2 Å and bond strengths of ∼20 kJ mol^{-1}. Hydrogen bonds contribute to the flexibility and functionality of biological matter, and di-hydrogen bonds appear as a new tool for the rational design of functional materials. The analogue compound, $MgCl_2 \cdot 2NH_3$, was also investigated. It lacks a network of dihydrogen bonds and is classified as an insulator. This new ligand-assisted cationic conductivity mechanism is denoted *pas-de-deux*, due to the simultaneous translation of an 'Mg^{2+}–NH_3 couple' as a part of the cationic migration pathway.

Furthermore, $Mg(BH_4)_2 \cdot xNH_3$ composites formed by non-integer *x*–values, i.e. physical mixtures of two compounds $Mg(BH_4)_2 \cdot xNH_3$ with different *x*–values, exhibited orders of magnitude higher conductivity than those of the individual compounds with integer *x*–values [155]. It was found that the composite $0.5Mg(BH_4)_2 \cdot NH_3$–$0.5Mg(BH_4)_2 \cdot 2NH_3$ is eutectically melting at $T = 55$ °C and that the molten state can be stabilised by nano-particles. A composite mechanochemically prepared from 0.4 $Mg(BH_4)_2 \cdot NH_3$–0.6 $Mg(BH_4)_2 \cdot 2NH_3$ with 75 wt% MgO nanoparticles, denoted $Mg(BH_4)_2 \cdot 1.6NH_3$-MgO displayed the highest conductivity with $\sigma(Mg^{2+}) = 2.1 \times 10^{-3}$ S cm^{-1} at $T = 55$ °C [155]. Interestingly, the high conductivity is stabilized to lower temperatures $\sigma(Mg^{2+}) = 1.2 \times 10^{-5}$ S cm^{-1} at RT and $\sigma(Mg^{2+}) = 5.0 \times 10^{-4}$ S cm^{-1} at $T = 60$ °C [155]. The nanoparticles prevent recrystallization of the highly dynamical amorphous state, which is stabilized over a long period of time, i.e. at least several months. The composite has high mechanical stability and can be heated to 200 °C without burning in air. ^{11}B solid-state NMR reveals that the composite is a mixture of the two parent compounds prior to heating. After heating the sample above 55 °C, the resonances for the BH_4 groups in the parent compounds are substituted by a single sharp resonance at a higher chemical shift. The significantly smaller full width at half maximum (FWHM) of the sharp resonance is indicative of higher dynamics in the composite after heating and suggests a stabilization of the molten state to room temperature, which is consistent with the high ionic conductivity [155].

Magnesium borohydride amidoborane, $Mg(BH_4)_2(NH_3BH_3)_2$, was recently discovered to be a promising electrolyte [161, 162]. Magnesium is tetrahedrally coordinated to two borohydride BH_4^- complexes and two

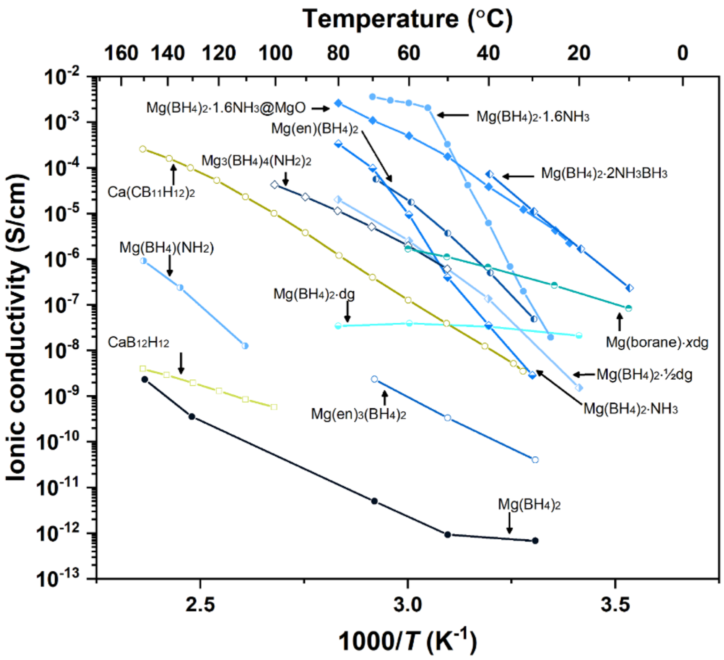

Figure 10. Calcium and magnesium ionic conductivity as a function of the temperature of known complex hydrides. Abbreviations: en (ethylene diamine), dg (diglyme), borane refer to a mixture of $B_{12}H_{12}^{2-}$, $B_{11}H_{11}^{2-}$ and $B_{11}H_{14}^{2-}$ [153, 155–161].

neutral ammonia borane (NH_3BH_3) molecules forming a distorted asymmetric Mg^{2+} coordination [163]. The compound $Mg(BH_4)_2(NH_3BH_3)_2$ is mechanochemically synthesized from $Mg(BH_4)_2$ and NH_3BH_3, and the Mg^{2+} ionic conductivity was measured by impedance spectroscopy to $\sigma(Mg^{2+}) = 1.3 \times 10^{-5}$ S cm^{-1} at 30 °C and $\sigma(Mg^{2+}) = 8.4 \times 10^{-5}$ S cm^{-1} at 40 °C, which are among the highest Mg^{2+} ionic conductivities reported for solid inorganic materials. In addition, electrochemical cells fabricated with $Mg(BH_4)_2(NH_3BH_3)_2$ as the solid electrolyte demonstrated reversible Mg migration through the material. These results, therefore, confirm that Mg^{2+} ionic conduction can be achieved by the coordination of NH_3BH_3 to $Mg(BH_4)_2$, and it is expected that these observations will contribute to the development of all-solid-state Mg batteries.

Furthermore, $Mg(BH_4)(NH_2)$ was also discovered as new type of magnesium electrolyte, with conductivity of $\sigma(Mg^{2+}) = 1 \times 10^{-6}$ S cm^{-1} at 150 °C [156]. Further investigation of the $Mg(BH_4)_2$ $Mg(NH_2)_2$ binary system revealed a glass-ceramic material containing an unidentified additional amorphous phase with improved conductivity of $\sigma(Mg^{2+}) = 3 \times 10^{-6}$ S cm^{-1} at 100 °C. Analysis of the $Mg(BH_4)_2$ $Mg(NH_2)_2$ phase diagram revealed the existence of a new compound $Mg_3(BH_4)_4(NH_2)_2$ with high thermal stability and decomposition at $T < 190$ °C, and high Mg^{2+} ionic conductivity, $\sigma(Mg^{2+}) = 4.1 \times 10^{-5}$ S cm^{-1} at 100 °C and low activation energy, $E_a = 0.84$ eV [164].

5.3. Electrolytes based on higher borates

Above, we discussed the smallest borate anion, tetrahydridomonoborate, BH_4^-, but several others also exist. Several cationic materials are described based on the octahydridotriborate anion, $B_3H_8^-$, which has attracted attention in order to develop new electrolytes for SSBs [7, 165]. The potassium analogue has interesting polymorphism, e.g. a second-order transition from monoclinic (α) to an orthorhombic α'–KB_3H_8 at 15 °C and a first-order transition to the cubic β–KB_3H_8 at 30 °C. The β-polymorph of KB_3H_8 displays a high degree of anionic disorder and cation mobility, $\sigma(K^+) \sim 10^{-7}$ S cm^{-1} above 100 °C [7]. An approximate two orders-of-magnitude increase of reorientational dynamics of $[B_3H_8]^-$ observed by neutron scattering for the α'– to β–KB_3H_8 transition is associated with a significant increase of the K^+ conductivity [166]. Potassium octahydridotriborate, β-KB_3H_8 decomposes at 160 °C to KBH_4 and $K_2B_{12}H_{12}$, which form $K_3(BH_4)(B_{12}H_{12})$ and display an even higher ionic conductivity [7, 167].

New silver *closo*-borates were discovered, $Ag_2B_{10}H_{10}$ and $Ag_2B_{12}H_{12}$, with high Ag^+ ion conductivity that are also semiconductors (bandgap ~ 2.3 eV). The room temperature structures (α) are ordered whereas the high-temperature polymorphs (β), $T > {\sim}200$ °C, show both cation and anion disorder. Disordered high-temperature polymorphs are usually associated with a stepwise increase of conductivity. In this case the disordered structure is efficiently stabilized to room temperature by anion substitution, to form

$Ag_{(2+x)}I_xB_{10}H_{10}$ and $Ag_{(2+x)}I_xB_{12}H_{12}$, possibly with $x \sim 1$, and with high Ag^+ conductivity up to 3.2 mS cm^{-1} at room temperature [168]. Solid-state ^1H and ^{11}B nuclear magnetic resonance spectroscopy identified two dynamic processes at low temperatures ($70 < T < 400$ K), involving dynamics of $B_{12}H_{12}{}^{2-}$ cages. One is relatively fast with $E_a = 308$ meV and the other is slower $E_a = 67$ meV. The fast rotations are associated with the diffusion of Ag^+ ions (the activation energy of cation jumps is $E_a = 482$ meV) [169].

Metal *closo*-borates have been useful as new monovalent cationic conductors, however, appear significantly less successful in generating new divalent cationic electrolytes. A series of metal decahydro-*closo*-decaborates, $MB_{10}H_{10}$ (M = Ca, Sr, and Mn) all have rather low ionic conductivity [170, 171].

The *closo*-monocarborate anions, with charge (−1), are a newly discovered class of electrolytes, not yet fully explored. The calcium *closo*-monocarborate salt, $Ca(CB_{11}H_{12})_2$ was originally developed as a highly stable and efficient Ca^{2+} liquid electrolyte for room-temperature calcium batteries [159]. In addition to superior electrochemical performance as Ca^{2+} liquid electrolyte, the electrochemical impedance measurements using pressed salt powder show a conductivity $>10^{-5}$ S cm^{-1} at 150 °C, higher than other systems [172]. Thus, this calcium *closo*-monocarborate $Ca(CB_{11}H_{12})_2$ will be developed not only as a liquid electrolyte but also as a solid-state electrolyte.

5.4. Dynamics in solid-state boron-based materials

The alkaline earth metal borohydrides, especially $Mg(BH_4)_2$, have a large number of polymorphs with interesting and different structures [173–175]. However, all polymorphs contain ideal $BH_4{}^-$ tetrahedra and similar coordination of magnesium to four borohydride complexes by edge sharing and almost linear H_2BH_2–Mg–H_2BH_2 chains. To date, the dynamics in $Mg(BH_4)_2$ have been investigated of the α–, β–, γ–, and amorphous modification [176]. Nevertheless, the dynamic properties of all four polymorphs show distinct differences as demonstrated by QENS [177–179]. QENS data, $S(Q, \hbar\omega)$ at ~300 K, of α–, β–, and γ–polymorphs reveal a very broad quasi-elastic signal of the high temperature β–polymorph, while α– and γ–$Mg(BH_4)_2$ exhibit a rather weak quasi-elastic signal, with almost no broadening around the elastic line. Thus, it can be concluded that the broad signal of β- is due to the thermally activated dynamics of the $BH_4{}^-$ tetrahedra around their symmetry axis (either C_2 or C_3), which can be assigned to the paddlewheel conductivity mechanism [180]. Furthermore, when comparing the γ–polymorph and the amorphous phase [176], it is rather obvious that in the latter the paddlewheel effect obviously plays a role. Here, the γ–polymorph shows almost no stochastic motions and no broadening around the elastic line, but the amorphous $Mg(BH_4)_2$ shows a significant broadening, which can be explained by the higher rotational movement of the $BH_4{}^-$ tetrahedra [176]. Thus, the paddlewheel effect seems responsible not only for the higher rotational movement but also for a higher Mg-ion conductivity, which can be supported by EIS measurements with the amorphous phase having two orders of magnitude higher conductivity at 80 °C. At 100 °C, the former rotating $BH_4{}^-$ became inactive caused by the crystallization reaction from amorphous to γ-$Mg(BH_4)_2$ [176].

Excellent utilization of QENS and solid-state NMR techniques for studying dynamics is illustrated by the investigation of the Mg^{2+} electrolyte $Mg(BH_4)_2$-½dg. In this case, both QENS and NMR reveal two non-equivalent $BH_4{}^-$ complexes, one slowly rotating population and another population that undergoes isotropic jump reorientations around the C_2/C_3 symmetry axes of $BH_4{}^-$. Both techniques quantify the two dynamically different $BH_4{}^-$ populations as a 1:1 ratio. NMR also reveals narrow resonances, again indicative of high $BH_4{}^-$ dynamics. Additionally, with the phase transition of the compound, QENS reveals a significant acceleration of the slow $BH_4{}^-$ group and the parameters describing segmental dynamics of the ethereal chain of diglyme show a steplike increase corresponding to enhanced flexibility. While the flexibility of diglyme is increased, the planar configuration coordinating one Mg^{2+} is retained. Greater flexibility in the system and higher dynamics of $BH_4{}^-$ facilitate high ionic conductivity. However in this case, the inhibited dynamics of one of the $BH_4{}^-$ populations may be the reason for the enhanced thermal stability as compared to $Mg(BH_4)_2$-dg [181]. Thus, it is possible to retain the enhancing effects of the chelating ligand on the ionic conductivity while improving the thermal stability [158].

6. Full SSBs using superionic conductor complex hydride electrolytes

As described above, complex hydrides have demonstrated promising properties as solid-state electrolyte (SSE) and have been implemented in different batteries cells. Different cathode materials have been used to assemble complete cells, and can be divided in (a) low voltage cathodes (<3V vs. Li/Li^+), e.g. sulfur and TiS_2, and (b) high voltage cathodes (>3V vs. Li/Li^+), e.g. $LiCoO_2$ and NMC. As reported in the following, complex hydrides result stable both in contact with low voltage cathode, forming a stable solid-electrode-interface (SEI) in some cases, and with high voltage cathode, when the $LiNbO_3$ buffer layer is used.

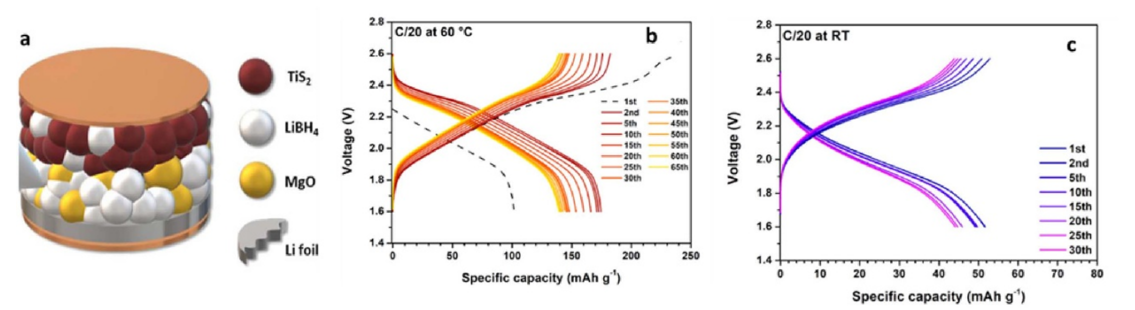

Figure 11. (a) Schematic of the prepared all-solid-state battery: Li|$LiBH_4$/MgO|TiS_2 battery. Voltage profiles at different cycles for a rate of 0.05 °C at (b) 60 °C, and (c) room temperature (25 °C). Reproduced from [91]. CC BY 4.0.

6.1. $LiBH_4$ based electrolytes

6.1.1. $Li_4(BH_4)_3I$

Different all-solid-state Li batteries using $Li_4(BH_4)_3I$ as SSE have been reported in the past years. Recently, a Li|$Li_4(BH_4)_3I$ |S cell has been reported, exhibiting a 43% capacity retention rate after 100 cycles [182]. The capacity fading mechanism has been investigated by cross-sectional SEM images comparing cells before and after the cycling tests. A combination of Raman spectroscopy and XRD analysis revealed that the solid electrolyte decomposed at a constant rate during the tests. Finally, the cathode mixture composition (S-C-SSE) has been optimized considering the capacity retention difference after 20 cycles.

6.1.2. $LiBH_4$–LiCl–P_2S_5

A novel solid-state electrolyte, with $(LiBH_4)_{0.73}(LiCl)_{0.24}(P_2S_5)_{0.03}$ approximate nominal composition and usable conductivity range for applications in solid state batteries has been reported [103]. During the preliminary electrochemical tests, this new SSE showed a stable interface contact with Li metal anode and TiS_2 cathode. The Li|SSE|TiS_2 cell showed a capacity retention of 93% of the theoretical capacity of TiS_2 (239 mAh g^{-1}) after ten cycles, with high and stable CE. An *operando* PXD analysis in transmission mode on the all-solid-state battery demonstrated that the (de)lithiation processes can be followed during the battery cycling tests [103].

6.1.3. $Li_6PS_5Z_{0.83}(BH_4)_{0.17}$, (Z = Cl, I)

The new class of $(BH_4)^-$ substituted argyrodites $Li_6PS_5Z_{0.83}(BH_4)_{0.17}$, ($Z$ = Cl, I) has been studied as RT solid-state electrolyte using both NMC ($LiNi_{1/3}Mn_{1/3}Co_{1/3}O_2$) and TiS_2 cathodes with In-Li anodes [183]. The use of NMC leads to interfacial reaction at the cathode side. Using a TiS_2 cathode, though presenting lower voltage, a higher capacity was achieved and full reversibility of the cathode was observed and preserved upon cycling with CE above 97%. Excellent electrochemical performance found for the TiS_2 cell evidenced better compatibility between the active material and the sulfide electrolyte in comparison to NMC. About 239 mAh g^{-1} at RT (i.e. the nominal capacity of TiS_2) has been obtained during the first charge/discharge cycle, despite the need for two to three activation cycles related to the SEI formation. Then, the battery provided full capacity for more than 35 cycles.

6.1.4. $LiBH_4$−MgO

The electrochemical properties of the optimized composition in the $LiBH_4$–MgO (i.e. 53 v/v % of MgO) composite SSE were tested in a battery cell, using TiS_2 and Li as a positive and negative electrode, respectively [91]. The Li| $LiBH_4$–MgO |TiS_2 cell has been cycled at 60 °C and with C rate of C/20 (figure 11). The cell showed a discharge capacity retention of more that 80% after 65 cycles. A discharge capacity of 175 mAh g^{-1} during the second cycle has been reported, corresponding to about 73% of the theoretical capacity of TiS_2. A self-discharge reaction during the first discharge cycle was reported and attributed to the formation of $Li_2B_{12}H_{12}$ SEI. After the 30th cycle, a pronounced decrease of the capacity is observed (i.e. discharge capacity of 174, 147 and 139 mAh g^{-1} for the 2nd, the 30th and the 65th cycle, respectively). This behaviour was attributed to two events: (a) the achievement of the maximal SEI thickness at 30th cycle, and (b) the fact that the cell was not supported by an appropriate stack pressure, likely leading to a continuous loss of contact at the electrodes-electrolyte interfaces. Additionally, after 65 cycles performed at 60 °C, the temperature of the test for the Li|CE53|TiS_2 cell was decreased to room temperature. The battery cell successfully operates at RT for more than 30 cycles, with a discharge capacity retention of 80%.

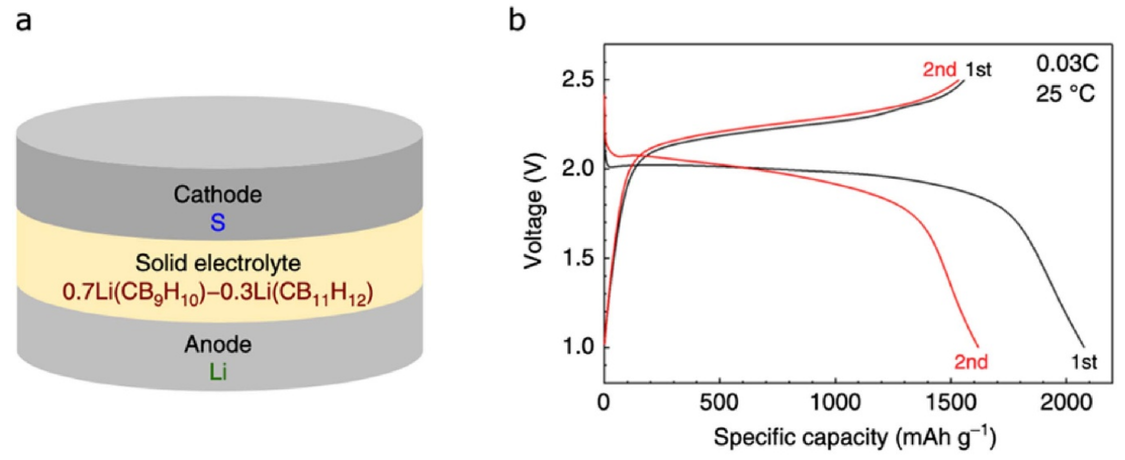

Figure 12. (a) Schematic illustration of the prepared all-solid-state batteries. Sulfur/$0.7Li(CB_9H_{10})$–$0.3Li$ $(CB_{11}H_{12})$, and lithium metal were used as the cathodes, solid electrolytes, and anodes, respectively. (b) Voltage profiles for a rate of 0.03 C at 25 °C during the first two cycles. Reproduced from [108]. CC BY 4.0.

6.2. Closoboranes based solid electrolytes

6.2.1. $Li(CB_9H_{10})-Li(CB_{11}H_{12})$

Solid-state lithium-sulfur battery employing $0.7Li(CB_9H_{10})$–$0.3Li(CB_{11}H_{12})$ as the solid electrolyte (figure 12(a)) show high performances over repeated discharge-charge cycles as shown in figure 12(b) [108]. After the first discharge, reversible charge–discharge profiles, which display a charge plateau at ∼2.2 V and a discharge plateau at ∼2.0 V, were observed. The discharge capacity in the second cycle was 1618 mAh g^{-1}, which corresponds to 96.8% of the theoretical capacity. The stability with lithium metal of $0.7Li(CB_9H_{10})$–$0.3Li(CB_{11}H_{12})$ coupled with its high ionic conductivity enables the excellent performance of high energy-density lithium-sulfur batteries in a wide temperature range. After the first discharge, reversible charge–discharge profiles, which present a charge plateau at ∼2.2 V and a discharge plateau at ∼2.0 V, were observed. The discharge capacity in the second cycle was 1618 mAh g^{-1}, which corresponds to 96.8% of the theoretical capacity. The stability with lithium metal of $0.7Li(CB_9H_{10})$–$0.3Li(CB_{11}H_{12})$ coupled with its high ionic conductivity enables the excellent performance of high energy-density lithium-sulfur batteries in a wide temperature range. Further work is devoted in obtaining a better understanding of the capacity fading mechanism of the battery systems using this complex hydride solid electrolyte by analyzing the cathode microstructure as demonstrated recently [182].

The compound $0.7Li(CB_9H_{10})$–$0.3Li(CB_{11}H_{12})$, was also studied as an SSE in a Li–TiS_2 battery [107]. The chemical stability between the solid electrolyte and a TiS_2 cathode was investigated, combining XRD and heat treatment demonstrating high chemical stability between these materials. After the first cycle, as the C-rate increased by 2, 5, 10, 20, 50, and 100 times from 0.1 C, the all-solid-state cell retained respective capacities of 96.3%, 93.4%, 90.8%, 85.3%, 80.2%, and 73.4% in the second cycle. The all-solid-state battery also exhibited superior cycling performance, i.e. at 0.2 C after 40 cycles, the capacity retention was 73.2% The CE during cycling became saturated at ∼100%.

6.2.2. $Li(BH_4)$–$B_{10}H_{14}$

A novel *closo*-type complex hydride solid electrolyte has been synthesized by heat and mechanochemical treatments of $LiBH_4$ and $B_{10}H_{14}$ in a 3:1 molar ratio. It was shown that the introduction of a $LiNbO_3$ buffer layer suppresses the side reactions at the cathode/SSE interface and improves charge–discharge performance of the all-solid-state Li–$LiCoO_2$ batteries with the *closo*-type complex hydride electrolyte. A decrease of the interfacial resistance of ∼10 times was achieved by using a 5 nm thick $LiNbO_3$ buffer layer. At 0.05 C, the discharge capacity of the cell was 103.2 mAh g^{-1} in the first cycle, and 75.2% of the capacity was retained after 20 cycles [184].

6.3. Other systems (Mg and Ca)

Magnesium borohydride and its complexes have displayed good anode compatibility [149, 155]. However, only a few examples have been reported for full cell batteries with Mg-containing complex hydrides solid-state electrolytes. Thus, further results on full battery cells are necessary to establish the compatibility between magnesium borohydride complexes and the electrodes, and in particular, the cathodes.

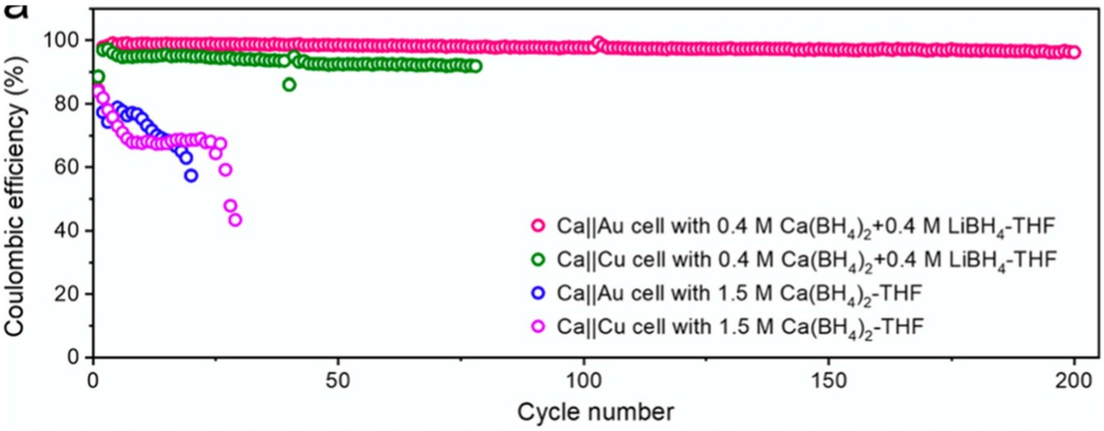

Figure 13. CE values of Ca | | Au and Ca | | Cu coin cells using $Ca(BH_4)_2$–$LiBH_4$–THF and $Ca(BH_4)_2$–THF electrolytes at 1 mA cm^{-2} and 0.5 mAh cm^{-2}. [188] John Wiley & Sons. [© 2020 Wiley-VCH Verlag GmbH & Co. KGaA, Weinheim].

The low electrochemical stability window of the borohydride (∼1.6 V vs Mg^{2+}/Mg) can be an issue for full cell cycling and stability vs high-capacity cathodes and similar strategies as sulfide-based ionic conductors may need to be implemented. This includes the development of cathode coatings for Mg-ion or bi-layered cell assembly with a suitable Mg catholyte. Halide based catholytes which are currently showing promising results for Li-based systems may not be an option in Mg-based systems as Mg-X complexes have been shown to inhibit cathode intercalation and limit the capacity [185, 186].

Based on the divalent cation Ca^{2+}, calcium-metal batteries (CMB) are attracting increasing attention as a high-energy and low-cost alternative compared to state-of-the-art LIB. Calcium is the fifth most abundant element in the Earth's crust, and is an ideal choice as an anode, with a low reduction potential of Ca metal (−2.87 V vs standard hydrogen electrode) and a high theoretical volumetric capacity of 2073 mAh cm^{-3}. Main challenges for CMB are related to the poor reversibility of Ca-metal anodes due to the formation of passivation layers with the traditional nonaqueous electrolytes which hinder the plating/stripping of Ca metal at room temperature. Inspired by the reports of boron-hydrogen electrolytes in Mg battery, recent studies have shown similar strategies for the development of practical Ca-based batteries. In particular, we highlight here two studies where electrolytes based on $Ca(BH_4)_2$–THF and $Ca(BH_4)_2$–$LiBH_4$–THF showed remarkable advancements.

In 2018 Wang *et al* [187] reported the first room-temperature Ca plating/stripping using $Ca(BH_4)_2$–THF, with Coulombic efficiencies (CE) of 94%–96% and a lifespan of ca. 50 cycles. In this system, thick films of calcium are deposited during plating, with small fractions of Ca and CaH_2 after each stripping process. The formation of the by-product CaH_2, instead of the usual products of calcium oxidation, does not inhibit plating and stripping, however it still acts as a protection layer mitigating further reaction of calcium with the electrolyte. Furthermore, CaH_2 does not function as an SEI layer on calcium, hence it does not allow the 99.98% desired level of cycling efficiency of a metal anode.

Jie *et al* [188] showed that by adding $LiBH_4$ in the $Ca(BH_4)_2$–THF, the electrolyte solvation structure is significantly changed, significantly improving the reversible plating and stripping of Ca metal at room temperature. The introduction of Li^+ decreases the coordination number of oxygens in the first solvation shell of Ca^{2+}, thus lowering the solvation energy. This should improve the kinetics of the desolvation process of Ca^{2+} at the electrode/electrolyte interface and may explain the obtained unprecedented average CE of 97.6% and long-term cycling stability over 200 cycles, as shown in figure 13. Results of Ca plating/stripping on Au or Cu electrodes indicate that the choice of the substrate impacts the cycling performances, with Au giving better values. For comparison, the CE of the Ca-metal anode with $Ca(BH_4)_2$–THF electrolyte shows fluctuations and rapid decay on both Au and Cu electrodes (figure 13). The morphology analysis of the deposits on the electrodes using the two electrolytes revealed two different results. In the case of $Ca(BH_4)_2$–$LiBH_4$–THF electrolyte, microsized spherical particles of Ca are deposited, with a reduced possibility to penetrate the separator and cause short circuit. Instead, with $Ca(BH_4)_2$–THF the deposit of Ca penetrates the separator and loses contact with the electrode, which may explain the limited cyclability.

In addition, a highly stable Ca electrolyte based on a monocarborane anion has been recently reported for room-temperature Ca batteries. The $Ca(CB_{11}H_{12})_2$ salt exhibited low solubilities in THF and DME, but high solubility in the mixed solvent of DME/THF (1/1, v/v %). The 0.5 M solution showed high conductivity, wide voltage window, and reversible Ca plating/stripping behavior with high CE. In addition, a Ca–S battery has been assembled using this electrolye, showing a high capacity of 805 mAh g^{-1}. This demonstrates that the electrolyte is compatible with a Ca–S battery system [159].

7. Conclusions and outlook

Metal and complex hydrides show outstanding properties for electrochemical energy storage applications. Initially developed for alkaline batteries of the NiMH type, the pioneering hydride forming intermetallics such as $LaNi_5$ have been progressively replaced by materials with more and more complex chemistries to meet the growing needs of users: autonomy, power and low cost. Today, this technology keeps its market share, and research remains very active to develop new generations of alloys to meet these needs. New approaches are also being considered, such as the use of new electrolytes. Meng *et al* [189] proposed recently to replace concentrated aqueous potash by aprotic ionic liquids mixed with acetic acid to limit metal corrosion detrimental for cycle life. Similarly, Shen *et al* [35] demonstrated that dioxygen addition allowed to rebalance the electrodes and restock the electrolyte by water reformation with H_2. Uesato *et al* [190] also showed that a sealed Ni–MH/Ni–H_2 hybrid cell can operate under hydrogen pressure up to 3 MPa. The charging of the battery proceeds by the hydrogenation of the anode by electrochemical and solid-gas reactions leading to a 50% gain in specific energy for the battery.

Beside alkaline battery, the proof of concept of metal hydride anodes useable for ion-batteries (Li- or Na-ion) has been made. Though still in itsearly stage, the conversion reaction process has been demonstrated for half-cells and complete battery systems [12, 42]. Although much higher capacity than graphite has been achieved, these systems suffer from slow kinetics, high operating temperature, and short lifetimes. These limitations call for new research to provide solutions using innovative geometries (nanostructuring, thin films, composites).

The degree of maturity of hydrides as solid electrolytes depends on the different battery chemistries. Monovalent Li and Na have already reached high technological levels. For Li and Na ASSBs, the main hurdle is the high cost of *closo*-borate electrolytes, related to the handling of toxic gases such as diborane and decaborane, but promising synthetic routes starting from cheaper Li(Na)BH_4 have been established [191–194]. In the case of Li, there are two approaches for conductivity enhancement: the complex anion substitution to stabilizing high-temperature structure and interface engineering by nano-confinement or ball-milling with oxides. Research has shown the combination of the two can further increase ionic conductivity [93, 94]. Similar concept is applicable to other Li complex hydrides and could be a promising approach to achieve high room temperature ionic conductivity for SSB application.

The large class of boron based complex metal hydrides has expanded significantly after the millennium and revealed extreme structural and compositional diversity with the discovery of a wide range of new materials. This class of materials typically has relatively directional bonding, i.e. polar covalent. They are also built by both relatively strong ionic or polar-covalent bonds as well as weak di-hydrogen bonds. Furthermore, borates can have a variety of coordination's to metals, e.g. BH_4^- (κ^1, κ^2, or κ^3) [195]. This has led to extreme structural flexibility and a new mechanism for cation conductivity denoted a ligand-assisted mechanism (or *pas-de-deux*) discussed in chapters 4 and 5 for $Mg(BH_4)_2{\cdot}NH_3$ and $LiBH_4{\cdot}{}^1\!/_2NH_3$ [84, 154]. This mechanism appears to be general for both mono- and divalent metal ions and may also account for the fast cationic conductivity observed for other similar compounds. Further exploration of structural flexibility of new materials, e.g. metal borohydrides with different organic molecules as ligands and different degree of hydrophilic/hydrophobic properties, is expected to lead to a range of new promising electrolytes.

The highstructural and compositional diversity and structural flexibility is also well illustrated by a series of ammonium *closo*-borate ammines, $(NH_4)_2B_{10}H_{10}{\cdot}xNH_3$ ($x = 1/2$, $\alpha-1$ and $\beta-1$) and $(NH_4)_2B_{12}H_{12}{\cdot}xNH_3$ ($x = 1$ and 2) that were recently discovered. Structural investigations using x-ray diffraction and DFT optimisation reveal the existence of an ammonium-ammonia complex in the solid-state $N_2H_7^+$, i.e. NH_4^+–NH_3 [196],. However, the proton conductivity is low, $\sigma(H^+) \sim 10^{-9}$ S cm^{-1}, at room temperature. Molecular dynamics simulations reveal high mobility of hydrogen within the complex cation NH_3–H–NH_3^+ but limited mobility in the solid-state due to large distance between different cation complexes [196]. Future investigation of ammonium-ammonia complex hydrides with smaller anions in the structure has significant potential to create new functional proton conductors, which may be used for the development of new low-temperature fuel cells. Recent studies also reveal high reorientational dynamics in ammonium borohydride (NH_4BH_4) and also high compositional and structural diversity of ammonium metal borohydrides [197–199].

Data availability statement

No new data were created or analysed in this study.

Acknowledgments

This paper was realised within the framework of the Hydrogen Technology Collaboration Programme (TCP) of the International Energy Agency (IEA) in Task 40 'Energy storage and conversion based on hydrogen'.

Torben R Jensen acknowledges funding from independent research fund Denmark for technology and production, Solid-State Magnesium Batteries—SOS-MagBat (9041-00226B) and Calcium Metal Battery—CaMBat (DFF—0217-00327B), and the Danish Ministry of Higher Education and Science through the SMART Lighthouse.

Rana Mohtadi is grateful for Mr Ryuta Sugiura and Dr Oscar Tutusaus at Toyota Research Institute of North America for the discussions and acknowledges the financial support from Toyota Motor Corporation.

Sabrina Sartori acknowledges the financial support from the European Union´s Horizon 2020 research and innovation program, under Grant Agreement No. 951815.

Brandon C Wood indicates that a portion of this work was performed under the auspices of the U.S. Department of Energy under Contract BW: DE-AC52-07NA27344. Computing resources were provided under the Innovative and Novel Computational Impact on Theory and Experiment (INCITE) program using resources of the Argonne Leadership Computing Facility, a U.S. Department of Energy Office of Science User Facility supported under Contract DE-AC02-06CH11357.

Mark Paskevicius acknowledges funding from the Australian Research Council (ARC) for an ARC Future Fellowship (FT160100303).

Kasper T Møller acknowledges funding from The Carlsberg Foundation (Grant CF19-0465).

Petra de Jongh and Peter Ngene acknowledges funding from NWO Netherlands materials for sustainability (739.017.009) grant; and NWO ECHO (712.015.005) grant.

Volodymyr Yartys acknowledges a support which this work received from the EU Horizon 2020 program in the H2020-MSCARISE-2017 action, HYDRIDE4MOBILITY project, with Grant Agreement 778307.

Dag Noreus acknowledges Yang Shen at Nilar AB for supplying figure 4 based on data from Nilar.

All authors are thankful to the International Energy Agency (Hydrogen Technology Collaboration Programme—Hydrogen TCP) Task-40 researchers for their inspired and inspirational work.

This manuscript honors the memory of our colleague Michel Latroche, who led and coordinated the process of writing this review, and suddenly passed away while the manuscript was under revision.

Fundings

NWO materials for sustainability (739.017.009) grant; and NWO ECHO (712.015.005) grant; RCN ENERGIX (LiMBAT 244054/E20); JSPS KAKENHI (17H06519 and 19K15666); JSPS KAKENHI (19K15305); JSPS KAKENHI (Hydrogenomics, JP18H05513); Hydrogen Materials–Advanced Research Consortium (HyMARC) of the U.S. Department of Energy (DOE), Office of Energy Efficiency and Renewable Energy, Hydrogen and Fuel Cell Technologies Office; U.S. Department of Energy (DOE), Office of Energy Efficiency and Renewable Energy, Vehicle Technologies Office under Contract DE-AC52-07NA27344; EU Horizon 2020 program, Grant Agreement 778307—HYDRIDE4MOBILITY—H2020-MSCA-RISE-2017; National Research Foundation of Korea (NRF-2020M1A2A2080881); ARC Future Fellowship FT160100303; Carlsberg Reintegration Fellowship CF19-0465.

ORCID iDs

Fermin Cuevas https://orcid.org/0000-0002-9055-5880
Mads B Amdisen https://orcid.org/0000-0003-2663-8988
Marcello Baricco https://orcid.org/0000-0002-2856-9894
Craig E Buckley https://orcid.org/0000-0002-3075-1863
Young Whan Cho https://orcid.org/0000-0001-9909-0082
Petra de Jongh https://orcid.org/0000-0002-2216-2620
Laura M de Kort https://orcid.org/0000-0001-5329-3087
Jakob B Grinderslev https://orcid.org/0000-0001-7645-1383
Valerio Gulino https://orcid.org/0000-0002-5808-7802
Bjørn C Hauback https://orcid.org/0000-0002-2717-6941
Michael Heere https://orcid.org/0000-0002-7826-1425
Terry Humphries https://orcid.org/0000-0003-1015-4495
Torben R Jensen https://orcid.org/0000-0002-4278-3221
Young-Su Lee https://orcid.org/0000-0002-3160-6633
Hai-Wen Li https://orcid.org/0000-0001-7223-1754

Rana Mohtadi https://orcid.org/0000-0002-1203-3809
Kasper T Møller https://orcid.org/0000-0002-1970-6703
Peter Ngene https://orcid.org/0000-0003-3691-0623
Dag Noréus https://orcid.org/0000-0001-5257-3909
Shin-ichi Orimo https://orcid.org/0000-0002-4216-0446
Mark Paskevicius https://orcid.org/0000-0003-2677-3434
Marek Polanski https://orcid.org/0000-0003-0163-514X
Sabrina Sartori https://orcid.org/0000-0002-9952-6488
Lasse N Skov https://orcid.org/0000-0001-5427-2632
Magnus H Sørby https://orcid.org/0000-0002-8878-3331
Volodymyr A Yartys https://orcid.org/0000-0003-4207-9127
Michel Latroche https://orcid.org/0000-0002-8677-8280

References

[1] European Union's Horizon 2020 *Battery 2030* (available at: https://battery2030.eu/research/roadmap/)
[2] Lebedeva N P and Boon-Brett L 2016 Considerations on the chemical toxicity of contemporary Li-ion battery electrolytes and their components *J. Electrochem. Soc.* **163** A821–30
[3] Goodenough J B 2013 Evolution of strategies for modern rechargeable batteries *Acc. Chem. Res.* **46** 1053–61
[4] Chu S, Cui Y and Liu N 2017 The path towards sustainable energy *Nat. Mater.* **16** 16–22
[5] Kato Y, Hori S, Saito T, Suzuki K, Hirayama M, Mitsui A, Yonemura M, Iba H and Kanno R 2016 High-power all-solid-state batteries using sulfide superionic conductors *Nat. Energy* **1** 16030
[6] Arthur T S *et al* 2017 Interfacial insight from operando XAS/TEM for magnesium metal deposition with borohydride electrolytes *Chem. Mater.* **29** 7183–8
[7] Grinderslev J B, Møller K T, Yan Y, Chen X M, Li Y, Li H W, Zhou W, Skibsted J, Chen X and Jensen T R 2019 Potassium octahydridotriborate: diverse polymorphism in a potential hydrogen storage material and potassium ion conductor *Dalton Trans.* **48** 8872–81
[8] Cuevas F, Joubert J-M, Latroche M and Percheron-Guégan A 2001 Intermetallic compounds as negative electrodes of Ni/MH batteries *Appl. Phys.* A **72** 225–38
[9] Joubert J-M, Paul-Boncour V, Cuevas F, Zhang J and Latroche M 2021 LaNi$_5$ related AB_5 compounds: structure, properties and applications *J. Alloys Compd.* **862** 158163
[10] Notten P H L, Ouwerkerk M, van Hal H, Beelen D, Keur W, Zhou J and Feil H 2004 High energy density strategies: from hydride-forming materials research to battery integration *J. Power Sources* **129** 45–54
[11] Yartys V, Noreus D and Latroche M 2016 Metal hydrides as negative electrode materials for Ni–MH batteries *Appl. Phys.* A **122** 1–11
[12] Sartori S, Cuevas F and Latroche M 2016 Metal hydrides used as negative electrode materials for Li-ion batteries *Appl. Phys.* A **122** 135
[13] Li H-W, Ikeda K, Nakamori Y, Orimo S, Yakushiji K, Takanashi K, Ohyama H, Nakatsuji K and Dansui Y 2007 Size distribution of precipitated Ni clusters on the surface of an alkaline-treated LaNi$_5$-based alloy *Acta Mater.* **55** 481–5
[14] Wan C, Denys R V and Yartys V A 2021 Towards understanding the influence of Mg content on phase transformations in the La3-xMgxNi9 alloys by *in-situ* neutron powder diffraction study *Prog. Nat. Sci.: Mater. Int.* **31** 698–704
[15] Crivello J-C, Zhang J and Latroche M 2011 Structural stability of ABy phases in the (La,Mg)–Ni system obtained by density functional theory calculations *J. Phys. Chem.* C **115** 25470–8
[16] Wan C, Hu W, Denys R V, Nwakwuo C C, Solberg J K and Yartys V A 2021 Effect of Mg content in the La3-xMgxNi9 battery anode alloys on the structural, hydrogen storage and electrochemical properties *J. Alloys Compd.* **856** 157443
[17] Nazer N S, Denys R V, Yartys V A, Hu W-K, Latroche M, Cuevas F, Hauback B C, Henry P F and Arnberg L 2017 In operando neutron diffraction study of LaNdMgNi9H13 as a metal hydride battery anode *J. Power Sources* **343** 502–12
[18] Charbonnier V, Madern N, Monnier J, Zhang J, Paul-Boncour V and Latroche M 2020 Thermodynamic and corrosion study of Sm$_{1\text{-}x}$Mg$_x$Ni$_y$ ($y = 3.5$ or 3.8) compounds forming reversible hydrides *Int. J. Hydrog. Energy* **45** 11686–94
[19] Zhang J, Charbonnier V, Madern N, Monnier J and Latroche M 2021 Improvement of reversible H storage capacity by fine tuning of the composition in the pseudo-binary systems $A_{2\text{-}x}$La$_x$Ni$_7$ ($A =$ Gd, Sm, Y, Mg) *J. Alloys Compd.* **852** 157008
[20] Young K-H, Nei J, Wan C, Denys R V and Yartys V A 2017 Comparison of C14- and C15-predomiated AB2 metal hydride alloys for electrochemical applications *Batteries* **3** 22
[21] Volodin A A, Denys R V, Wan C, Wijayanti I D, Suwarno S, Tarasov B P, Antonov V E and Yartys V A 2019 Study of hydrogen storage and electrochemical properties of AB2-type Ti0.15Zr0.85La0.03Ni1.2Mn0.7V0.12Fe0.12 alloy *J. Alloys Compd.* **793** 564–75
[22] Wan C, Denys R V and Yartys V A 2021 Effects of Ti substitution for Zr on the electrochemical characteristics and structure of AB2-type Laves-phase alloys as metal hydride anodes *J. Alloys Compd.* **889** 161655
[23] Wan C, Denys R V, Lelis M, Milčius D and Yartys V A 2019 Electrochemical studies and phase-structural characterization of a high-capacity La-doped AB2 Laves type alloy and its hydride *J. Power Sources* **418** 193–201
[24] Wijayanti I D, Mølmen L, Denys R V, Guzik M N, Gorsse S, Bobet J-L and Yartys V A 2021 Studies of the effect of melt spinning on the electrochemical properties of the AB2 Laves phase alloys *Int. J. Mech. Eng. Sci.* **5** 24–29
[25] Wijayanti I D, Mølmen L, Denys R V, Nei J, Gorsse S, Young K, Guzik M N and Yartys V 2020 The electrochemical performance of melt-spun C14-Laves type TiZr-based alloy *Int. J. Hydrog. Energy* **45** 1297–303
[26] Wijayanti I D, Denys R, Suwarno S, Volodin A A, Lototskyy M V, Guzik M N, Nei J, Young K, Roven H J and Yartys V 2020 Hydrides of Laves type Ti–Zr alloys with enhanced H storage capacity as advanced metal hydride battery anodes *J. Alloys Compd.* **828** 154354
[27] Wijayanti I D, Mølmen L, Denys R V, Nei J, Gorsse S, Guzik M N, Young K and Yartys V 2019 Studies of Zr-based C15 type metal hydride battery anode alloys prepared by rapid solidification *J. Alloys Compd.* **804** 527–37

[28] Lei Y, Wu Y, Yang Q, Wu J and Wang Q 1994 Electrochemical behaviour of some mechanically alloyed Mg—Ni-based amorphous hydrogen storage alloys *Z. Phys. Chem.* **183** 379–84

[29] Tian Q-F, Zhang Y, Chu H-L, Sun L-X, Xu F, Tan Z-C, Yuan H-T and Zhang T 2006 The electrochemical performances of Mg0.9Ti0.1Ni1−xPdx (x = 0–0.15) hydrogen storage electrode alloys *J. Power Sources* **159** 155–8

[30] Ye H, Lei Y Q, Chen L S and Zhang H 2000 Electrochemical characteristics of amorphous Mg0.9M0.1Ni (M = Ni, Ti, Zr, Co and Si) ternary alloys prepared by mechanical alloying *J. Alloys Compd.* **311** 194–9

[31] Huang J, Ouyang L, Wang H, Liu J, Zhu M, Fang F and Sun D 2019 Hydrogenation and crystallization of amorphous phase: a new mechanism for the electrochemical capacity and its decay in milled MgNi alloys *Electrochim. Acta* **305** 145–54

[32] Huang J, Wang H, Ouyang L, Liu J and Zhu M 2019 Reducing the electrochemical capacity decay of milled Mg–Ni alloys: the role of stabilizing amorphous phase by Ti-substitution *J. Power Sources* **438** 226984

[33] Huang J, Liao C, Wang H, Zhao Y, Ouyang L, Liu J and Zhu M 2022 Using tetramethylammonium hydroxide electrolyte to inhibit corrosion of Mg-based amorphous alloy anodes: a route for promotion energy density of Ni-MH battery *J. Alloys Compd.* **907** 164293

[34] Young K-H, Koch J M, Wan C, Denys R V and Yartys V A 2017 Cell performance comparison between C14- and C15-predomiated AB2 metal hydride alloys *Batteries* **3** 29

[35] Shen Y, Noréus D and Starborg S 2018 Increasing NiMH battery cycle life with oxygen *Int. J. Hydrog. Energy* **43** 18626–31

[36] Noréus D 2016 Metal hydride battery with added hydrogen gas, oxygen gas or hydrogen peroxide (https://doi.org/10.1021/acs.inorgchem.6b00074)

[37] Linden D 2002 Nickel-Hydrogen Batteries *Handbook of Batteries* 3rd edn (New York: McGraw Hill) ch 32

[38] Shen Y, Svensson Grape E, Noréus D, Widenkvist E and Starborg S 2020 Upcycling of spent NiMH battery material—reconditioned battery alloys show faster activation and reaction kinetics than pristine alloys *Molecules* **25** 2338

[39] Aymard L, Oumellal Y and Bonnet J-P 2015 Metal hydrides: an innovative and challenging conversion reaction anode for lithium-ion batteries *Beilstein J. Nanotechnol.* **6** 1821–39

[40] Silvestri L, Forgia S, Farina L, Meggiolaro D, Panero S, La Barbera A, Brutti S and Reale P 2015 Lithium alanates as negative electrodes in lithium-ion batteries *Chemelectrochem* **2** 877–86

[41] Dao A H, Berti N, López-Aranguren P, Zhang J, Cuevas F, Jordy C and Latroche M 2018 Electrochemical properties of MgH_2—TiH_2 nanocomposite as active materials for all-solid-state lithium batteries *J. Power Sources* **397** 143–9

[42] Latroche M *et al* 2019 Full-cell hydride-based solid-state Li batteries for energy storage *Int. J. Hydrog. Energy* **44** 7875–87

[43] Zeng L, Ichikawa T, Kawahito K, Miyaoka H and Kojima Y 2017 Bulk-type all-solid-state lithium-ion batteries: remarkable performances of a carbon nanofiber-supported MgH_2 composite electrode *ACS Appl. Mater. Interfaces* **9** 2261–6

[44] Cheng Q, Sun D and Yu X 2018 Metal hydrides for lithium-ion battery application: a review *J. Alloys Compd.* **769** 167–85

[45] Brutti S, Mulas G, Piciollo E, Panero S and Reale P 2012 Magnesium hydride as a high capacity negative electrode for lithium ion batteries *J. Mater. Chem.* **22** 14531–7

[46] Oumellal Y, Rougier A, Nazri G A, Tarascon J-M and Aymard L 2008 Metal hydrides for lithium-ion batteries *Nat. Mater.* **7** 916–21

[47] Teprovich J A, Zhang J, Colón-Mercado H, Cuevas F, Peters B, Greenway S, Zidan R and Latroche M 2015 Li-driven electrochemical conversion reaction of AlH_3, $LiAlH_4$, and $NaAlH_4$ *J. Phys. Chem.* C **119** 4666–74

[48] Berti N, Hadjixenophontosb E, Cuevas F, Zhang J, Lacoste A, Dubot P, Schmitz G and Latroche M 2018 Thin films as model system for understanding the electrochemical reaction mechanisms in conversion reaction of MgH_2 with lithium *J. Power Sources* **402** 99–106

[49] El Kharbachi A, Hu Y, Sørby M H, Vullum P E, Mæhlen J P, Fjellvåg H and Hauback B C 2018 Understanding capacity fading of MgH_2 conversion-type anodes via structural morphology changes and electrochemical impedance *J. Phys. Chem.* C **122** 8750–9

[50] Zeng L, Kawahito K, Ikeda S, Ichikawa T, Miyaoka H and Kojima Y 2015 Metal hydride-based materials towards high performance negative electrodes for all-solid-state lithium-ion batteries *Chem. Commun.* **51** 9773–6

[51] Cano-Banda F, Singh R, Hernandez-Guerrero A, Jain A and Ichikawa T 2021 Enhanced performance of MgH_2 composite electrode using glass-ceramic electrolytes for all-solid-state Li-ion batteries *J. Alloys Compd.* **863** 158729

[52] Huen P and Ravnsbæk D B 2018 All-solid-state lithium batteries—the Mg_2FeH_6-electrode $LiBH_4$-electrolyte system *Electrochem. Commun.* **87** 81–85

[53] Oumellal Y, Zaïdi W, Bonnet J-P, Cuevas F, Latroche M, Zhang J, Bobet J-L, Rougier A and Aymard L 2012 Reactivity of TiH_2 hydride with lithium ion: evidence for a new conversion mechanism *Int. J. Hydrog. Energy* **37** 7831–5

[54] Oumellal Y, Rougier A, Tarascon J-M and Aymard L 2009 2LiH +M (M = Mg, Ti): new concept of negative electrode for rechargeable lithium-ion batteries *J. Power Sources* **192** 698–702

[55] Kawahito K, Zeng L, Ichikawa T, Miyaoka H and Kojima Y 2016 Electrochemical performance of titanium hydride for bulk-type all-solid-state lithium-ion batteries *Mater. Trans.* **57** 755–7

[56] Rizo-Acosta P, Cuevas F and Latroche M 2018 Optimization of TiH2 content for fast and efficient hydrogen cycling of MgH2-TiH2 nanocomposites *Int. J. Hydrog. Energy* **43** 16774–81

[57] Huang L, Aymard L and Bonnet J-P 2015 MgH2–TiH2 mixture as an anode for lithium-ion batteries: synergic enhancement of the conversion electrode electrochemical performance *J. Mater. Chem.* A **3** 15091–6

[58] Berti N, Cuevas F, Zhang J and Latroche M 2017 Enhanced reversibility of the electrochemical Li conversion reaction with MgH2-TiH2 nanocomposites *Int. J. Hydrog. Energy* **42** 22615–21

[59] Hadjixenophontos E *et al* 2020 A review of the MSCA ITN ECOSTORE—novel complex metal hydrides for efficient and compact storage of renewable energy as hydrogen and electricity *Inorganics* **8** 17

[60] López-Aranguren P, Berti N, Dao H A, Zhang J, Cuevas F, Latroche M and Jordy C 2017 An all-solid-state metal hydride—sulfur lithium-ion battery *J. Power Sources* **357** 56–60

[61] Matsumura Y, Takagishi K, Miyaoka H and Ichikawa T 2019 Vanadium hydride as conversion type negative electrode for all-solid-state lithium-ion-battery *Mater. Trans.* **60** 2183–7

[62] Xu Y and Mulder F M 2018 TiF_3 catalyzed MgH_2 as a Li/Na ion battery anode *Int. J. Hydrog. Energy* **43** 20033–40

[63] Ren Y, Ren X, Ahuja R and Qian Z 2020 First-principles calculations into $LiAl(NH_2)_4$ and its derivative hydrides for potential sodium storage *Results Phys.* **19** 103408

[64] Hansen B R S, Paskevicius M, Li H-W, Akiba E and Jensen T R 2016 Metal boranes: progress and applications *Coord. Chem. Rev.* **323** 60–70

[65] Matsuo M and Orimo S 2011 Lithium fast-ionic conduction in complex hydrides: review and prospects *Adv. Energy Mater.* **1** 161–72

[66] Mohtadi R and Orimo S 2017 The renaissance of hydrides as energy materials *Nat. Rev. Mater.* **2** 16091

[67] Unemoto A, Matsuo M and Orimo S-I 2014 Complex hydrides for electrochemical energy storage *Adv. Funct. Mater.* **24** 2267–79

[68] Ikeshoji T, Tsuchida E, Morishita T, Ikeda K, Matsuo M, Kawazoe Y and Orimo S 2011 Fast-ionic conductivity of Li + in LiBH 4 *Phys. Rev.* B **83** 144301

[69] Soulie J-P and Renaudin G 2002 Lithium boro-hydride $LiBH_4$ I. Crystal structure *J. Alloys Compd.* **346** 200

[70] Verdal N, Udovic T J and Rush J J 2012 The nature of BH_4—reorientations in hexagonal $LiBH_4$ *J. Phys. Chem.* C **116** 1614–8

[71] Remhof A, Yan Y, Embs J P, Sakai V G, Nale A, de Jongh P, Łodziana Z and Züttel A 2015 Rotational disorder in lithium borohydride ed B Frick, M M Koza, M Boehm and H Mutka *EPJ Web Conf.* **83** 02014

[72] Aeberhard P C, Refson K and David W I F 2013 Molecular dynamics investigation of the disordered crystal structure of hexagonal LiBH4 *Phys. Chem. Chem. Phys.* **15** 8081

[73] Gulino V, Wolczyk A, Golov A A, Eremin R A, Palumbo M, Nervi C, Blatov V A, Proserpio D M and Baricco M 2020 Combined DFT and geometrical-topological analysis of Li-ion conductivity in complex hydrides *Inorg. Chem. Front.* **7** 3115–25

[74] Gulino V, Dematteis E M, Corno M, Palumbo M and Baricco M 2021 Theoretical and experimental studies of $LiBH_4$-LiBr phase diagram *ACS Appl. Energy Mater.* **4** 7327–37

[75] Gulino V, Brighi M, Dematteis E M, Murgia F, Nervi C, Cerny R and Baricco M 2019 Phase stability and fast ion conductivity in the hexagonal LiBH4-LiBr-LiCl solid solution *Chem. Mater.* **31** 5133–44

[76] Lee Y-S, Ley M B, Jensen T R and Cho Y W 2016 Lithium ion disorder and conduction mechanism in $LiCe(BH_4)_3)Cl$ *J. Phys. Chem.* C **120** 19035–42

[77] Ley M B, Ravnsbæk D B, Filinchuk Y, Lee Y-S, Janot R, Cho Y W, Skibsted J and Jensen T R 2012 $LiCe(BH_4)_3Cl$, a new lithium-ion conductor and hydrogen storage material with isolated tetranuclear anionic clusters *Chem. Mater.* **24** 1654–63

[78] Ley M B, Boulineau S, Janot R, Filinchuk Y and Jensen T R 2012 New Li ion conductors and solid state hydrogen storage materials: $LiM(BH_4)_3Cl$, M = La, Gd *J. Phys. Chem.* C **116** 21267–76

[79] Olsen J E, Frommen C, Jensen T R, Riktor M D, Sorby M H and Hauback B C 2014 Structure and thermal properties of composites with RE-borohydrides (RE = La, Ce, Pr, Nd, Sm, Eu, Gd, Tb, Er, Yb or Lu) and $LiBH_4$ *RSC Adv.* **4** 1570–82

[80] Soloninin A V, Babanova O A, Skoryunov R V, Skripov A V, Grinderslev J B and Jensen T R 2021 NMR study of the dynamical properties of $LiLa(BH_4)_3Br$ and $LiLa(BH_4)3I$ *Appl. Magn. Reson.* **52** 595–606

[81] Skripov A V, Majer G, Babanova O A, Skoryunov R V, Soloninin A V, Ley M B, Jensen T R, Orimo S and Udovic T J 2021 Lithium-ion diffusivity in complex hydrides: pulsed-field-gradient NMR studies of $LiLa(BH_4)_3Cl$, Li-3$(NH_2)_2$I and Li-1-CB_9H_{10} *Solid State Ion.* **362** 115585

[82] Oguchi H, Kim S, Maruyama S, Horisawa Y, Takagi S, Sato T, Shimizu R, Matsumoto Y, Hitosugi T and Orimo S 2019 Epitaxial film growth of $LiBH_4$ via molecular unit evaporation *ACS Appl. Eectron. Mater.* **1** 1792–6

[83] Blanchard D, Nale A C, Sveinbjörnsson D, Eggenhuisen T M, Verkuijlen M H W, Suwarno S, Vegge T, Kentgens A P M and de Jongh P E 2015 Nanoconfined $LiBH_4$ as a fast lithium ion conductor *Adv. Funct. Mater.* **25** 184–92

[84] Yan Y, Grinderslev J B, Lee Y S, Jørgensen M, Cho Y W, Černý R and Jensen T R 2020 Ammonia-assisted fast Li-ion conductivity in a new hemiammine lithium borohydride, $LiBH_4 \cdot 1/2NH_3$ *Chem. Commun.* **56** 3971–4

[85] Choi Y S, Lee Y-S, Oh K H and Cho Y W 2016 Interface-enhanced Li ion conduction in a $LiBH_4$-SiO_2 solid electrolyte *Phys. Chem. Chem. Phys.* **18** 22540–7

[86] Lambregts S, van Eck E, Suwarno S, Ngene P, de Jongh P and Kentgens A 2019 Phase behavior and ion dynamics of nanoconfined $LiBH_4$ in silica *J. Phys. Chem.* C **123** 25559–69

[87] Ngene P, Lambregts S, Blanchard D, Vegge T, Sharma M, Hagemann H and de Jongh P 2019 The influence of silica surface groups on the Li-ion conductivity of $LiBH_4/SiO_2$ nanocomposites *Phys. Chem. Chem. Phys.* **21** 22456–66

[88] Choi Y, Lee Y, Choi D, Chae K, Oh K and Cho Y 2017 Enhanced Li ion conductivity in $LiBH_4$-Al_2O_3 mixture via interface engineering *J. Phys. Chem.* C **121** 26209–15

[89] Lee Y and Cho Y 2017 Fast lithium ion migration in room temperature $LiBH_4$ *J. Phys. Chem.* C **121** 17773–9

[90] Gulino V, Barberis L, Ngene P, Baricco M and de Jongh P E 2020 Enhancing Li-ion conductivity in $LiBH_4$-based solid electrolytes by adding various nanosized oxides *ACS Appl. Energy Mater.* **3** 4941–8

[91] Gulino V, Brighi M, Murgia F, Ngene P, de Jongh P, Černý R and Baricco M 2021 Room-temperature solid-state lithium-ion battery using a $LiBH_4$–MgO composite electrolyte *ACS Appl. Energy Mater.* **4** 1228–36

[92] Zettl R, Hogrefe K, Gadermaier B, Hanzu I, Ngene P, De Jongh P and Wilkening H 2021 Conductor-insulator interfaces in solid electrolytes: a design strategy to enhance Li-ion dynamics in nanoconfined $LiBH_4/Al_2O_3$ *J. Phys. Chem.* C **125** 15052–60

[93] Zettl R, de Kort L, Gombotz M, Wilkening H M R, de Jongh P E and Ngene P 2020 Combined effects of anion substitution and nanoconfinement on the ionic conductivity of Li-based complex hydrides *J. Phys. Chem.* C **124** 2806–16

[94] Zettl R, Gombotz M, Clarkson D, Greenbaum S G, Ngene P, de Jongh P E and Wilkening H M R 2020 Li-ion diffusion in nanoconfined $LiBH_4$-LiI/Al_2O_3: from 2D bulk transport to 3D long-range interfacial dynamics *ACS Appl. Mater. Interfaces* **12** 38570–83

[95] de Kort L, Harmel J, de Jongh P and Ngene P 2020 The effect of nanoscaffold porosity and surface chemistry on the Li-ion conductivity of $LiBH_4$-$LiNH_2$/metal oxide nanocomposites *J. Mater. Chem.* A **8** 20687–97

[96] Takano A, Oikawa I, Kamegawa A and Takamura H 2016 Enhancement of the lithium-ion conductivity of $LiBH_4$ by hydration *Solid State Ion.* **285** 47–50

[97] Zhang T *et al* 2018 Ammonia, a switch for controlling high ionic conductivity in lithium borohydride ammoniates *Joule* **2** 1522–33

[98] Zhang R, Zhao W, Liu Z, Wei S, Yan Y and Chen Y 2021 Enhanced room temperature ionic conductivity of the $LiBH_4 \cdot 1/2NH_3$-Al_2O_3 composite *Chem. Commun.* **57** 2380–3

[99] Liu H, Ren Z, Zhang X, Hu J, Gao M, Pan H and Liu Y 2020 Incorporation of ammonia borane groups in the lithium borohydride structure enables ultrafast lithium ion conductivity at room temperature for solid-state batteries *Chem. Mater.* **32** 671–8

[100] Trinh N, Lepage D, Ayme-Perrot D, Badia A, Dolle M and Rochefort D 2018 An artificial lithium protective layer that enables the use of acetonitrile-based electrolytes in lithium metal batteries *Angew. Chem., Int. Ed.* **57** 5072–5

[101] Yamada Y, Furukawa K, Sodeyama K, Kikuchi K, Yaegashi M, Tateyama Y and Yamada A 2014 Unusual stability of acetonitrile-based superconcentrated electrolytes for fast-charging lithium-ion batteries *J. Am. Chem. Soc.* **136** 5039–46

[102] Moller K, Paskevicius M, Andreasen J, Lee J, Chen-Tan N, Overgaard J, Payandeh S, Silvester D, Buckley C and Jensen T 2019 Molten metal closo-borate solvates *Chem. Commun.* **55** 3410–3

[103] El Kharbachi A *et al* 2020 Pseudo-ternary $LiBH_4 \cdot LiCl \cdot P_2S_5$ system as structurally disordered bulk electrolyte for all-solid-state lithium batteries *Phys. Chem. Chem. Phys.* **22** 13872–9

[104] Kim S, Toyama N, Oguchi H, Sato T, Takagi S, Ikeshoji T and Orimo S 2018 Fast lithium-ion conduction in atom-deficient *closo*-type complex hydride solid electrolytes *Chem. Mater.* **30** 386–91

[105] Tang W S *et al* 2016 Liquid-like ionic conduction in solid lithium and sodium monocarba-*closo*-decaborates near or at room temperature *Adv. Energy Mater.* **6** 1502237

[106] Toyama N, Kim S, Oguchi H, Sato T, Takagi S, Tazawa M, Nogami G and Orimo S 2019 Lithium ion conductivity of complex hydrides incorporating multiple closo-type complex anions *J. Energy Chem.* **38** 84–87

[107] Kim S, Kisu K, Takagi S, Oguchi H and Orimo S 2020 Complex hydride solid electrolytes of the $Li(CB_9H_{10})$–$Li(CB_{11}H_{12})$ quasi-binary system: relationship between the solid solution and phase transition, and the electrochemical properties *ACS Appl. Energy Mater.* **3** 4831–9

[108] Kim S, Oguchi H, Toyama N, Sato T, Takagi S, Otomo T, Arunkumar D, Kuwata N, Kawamura J and Orimo S 2019 A complex hydride lithium superionic conductor for high-energy-density all-solid-state lithium metal batteries *Nat. Commun.* **10** 1081

[109] Kim S, Kisu K and Orimo S 2021 Stabilization of superionic-conducting high-temperature phase of $Li(CB_9H_{10})$ via solid solution formation with $Li_2(B_{12}H_{12})$ *Crystals* **11** 330

[110] Hansen B, Paskevicius M, Jørgensen M and Jensen T 2017 Halogenated sodium-closo-dodecaboranes as solid-state ion conductors *Chem. Mater.* **29** 3423–30

[111] Kweon K E, Varley J B, Shea P, Adelstein N, Mehta P, Heo T W, Udovic T J, Stavila V and Wood B C 2017 Structural, chemical, and dynamical frustration: origins of superionic conductivity in closo-borate solid electrolytes *Chem. Mater.* **29** 9142–53

[112] Li S, Qiu P, Kang J, Ma Y, Zhang Y, Yan Y, Jensen T, Guo Y, Zhang J and Chen X 2021 Iodine-substituted lithium/sodium closo-decaborates: syntheses, characterization, and solid-state ionic conductivity *ACS Appl. Mater. Interfaces* **13** 17554–64

[113] Jørgensen M, Jensen S, Humphries T, Rowles M, Sofianos M, Buckley C, Jensen T and Paskevicius M 2020 Hydroxylated closo-dodecaborates $M_2B_{12}(OH)_{12}$ (M = Li, Na, K, and Cs); structural analysis, thermal properties, and solid-state ionic conductivity *J. Phys. Chem.* C **124** 11340–9

[114] Jørgensen M, Hansen B, Lee Y, Cho Y and Jensen T 2019 Crystal structures and energy storage properties of ammine sodium decahydro-closo-decaboranes ($Na_2B_{10}H_{10}\cdot nNH_3$, n = 1, 2) *J. Phys. Chem.* C **123** 20160–6

[115] Jørgensen M *et al* 2020 Understanding superionic conductivity in lithium and sodium salts of weakly coordinating closo-hexahalocarbaborate anions *Chem. Mater.* **32** 1475–87

[116] Tang W S, Dimitrievska M, Stavila V, Zhou W, Wu H, Talin A and Udovic T 2017 Order-disorder transitions and superionic conductivity in the sodium nido-undeca(carba)borates *Chem. Mater.* **29** 10496–509

[117] Souza D H P, Møller K T, Moggach S A, Humphries T D, D'Angelo A M, Buckley C E and Paskevicius M 2021 Hydrated alkali-$B_{11}H_{14}$ salts as potential solid-state electrolytes *J. Mater. Chem.* A **9** 15027–37

[118] Payandeh S, Asakura R, Avramidou P, Rentsch D, Lodziana Z, Cerny R, Remhof A and Battaglia C 2020 Nido-borate/closo-borate mixed-anion electrolytes for all-solid-state batteries *Chem. Mater.* **32** 1101–10

[119] Payandeh S, Rentsch D, Łodziana Z, Asakura R, Bigler L, Černý R, Battaglia C and Remhof A 2021 Nido-hydroborate-based electrolytes for all-solid-state lithium batteries *Adv. Funct. Mater.* **31** 2010046

[120] Dimitrievska M, Shea P, Kweon K E, Bercx M, Varley J B, Tang W S, Skripov A V, Stavila V, Udovic T J and Wood B C 2018 Carbon incorporation and anion dynamics as synergistic drivers for ultrafast diffusion in superionic $LiCB_{11}H_{12}$ and $NaCB_{11}H_{12}$ *Adv. Energy Mater.* **8** 1703422

[121] Duchene L, Lunghammer S, Burankova T, Liao W, Embs J, Coperet C, Wilkening H, Remhof A, Hagemann H and Battaglia C 2019 Ionic conduction mechanism in the Na-2(B12H12)(0.5)(B10H10)(0.5) closo-borate solid-state electrolyte: interplay of disorder and ion-ion interactions *Chem. Mater.* **31** 3449–60

[122] Duchene L, Kuhnel R, Rentsch D, Remhof A, Hagemann H and Battaglia C 2017 A highly stable sodium solid-state electrolyte based on a dodeca/deca-borate equimolar mixture *Chem. Commun.* **53** 4195–8

[123] He L, Li H, Nakajima H, Tumanov N, Filinchuk Y, Hwang S, Sharma M, Hagemann H and Akiba E 2015 Synthesis of a bimetallic dodecaborate $LiNaB_{12}H_{12}$ with outstanding superionic conductivity *Chem. Mater.* **27** 5483–6

[124] Skripov A, Babanova O, Soloninin A, Stavila V, Verdal N, Udovic T and Rush J 2013 Nuclear magnetic resonance study of atomic motion in $A_2B_{12}H_{12}$ (A = Na, K, Rb, Cs): anion reorientations and Na^+ mobility *J. Phys. Chem.* C **117** 25961–8

[125] Tang W S, Unemoto A, Zhou W, Stavila V, Matsuo M, Wu H, Orimo S and Udovic T J 2015 Unparalleled lithium and sodium superionic conduction in solid electrolytes with large monovalent cage-like anions *Energy Environ. Sci.* **8** 3637–45

[126] Tang W S, Matsuo M, Wu H, Stavila V, Unemoto A, Orimo S and Udovic T J 2016 Stabilizing lithium and sodium fast-ion conduction in solid polyhedral-borate salts at device-relevant temperatures *Energy Storage Mater.* **4** 79–83

[127] Teprovich J, Colon-Mercado H, Washington A, Ward P, Greenway S, Missimer D, Hartman H, Velten J, Christian J and Zidan R 2015 Bi-functional $Li_2B_{12}H_{12}$ for energy storage and conversion applications: solid-state electrolyte and luminescent down-conversion dye *J. Mater. Chem.* A **3** 22853–9

[128] Udovic T, Matsuo M, Unemoto A, Verdal N, Stavila V, Skripov A, Rush J, Takamura H and Orimo S 2014 Sodium superionic conduction in $Na_2B_{12}H_{12}$ *Chem. Commun.* **50** 3750–2

[129] Verdal N, Udovic T, Stavila V, Tang W, Rush J and Skripov A 2014 Anion reorientations in the superionic conducting phase of $Na_2B_{12}H_{12}$ *J. Phys. Chem.* C **118** 17483–9

[130] Verdal N, Her J, Stavila V, Soloninin A, Babanova O, Skripov A, Udovic T and Rush J 2014 Complex high-temperature phase transitions in $Li_2B_{12}H_{12}$ and $Na_2B_{12}H_{12}$ *J. Solid State Chem.* **212** 81–91

[131] Boere R, Bolli C, Finze M, Himmelspach A, Knapp C and Roemmele T 2013 Quantum-chemical and electrochemical investigation of the electrochemical windows of halogenated carborate anions *Chem. Eur. J.* **19** 1784–95

[132] Asakura R, Reber D, Duchêne L, Payandeh S, Remhof A, Hagemann H and Battaglia C 2020 4 V room-temperature all-solid-state sodium battery enabled by a passivating cathode/hydroborate solid electrolyte interface *Energy Environ. Sci.* **13** 5048–58

[133] Duchene L, Remhof A, Hagemann H and Battaglia C 2020 Status and prospects of hydroborate electrolytes for all-solid-state batteries *Energy Storage Mater.* **25** 782–94

[134] Duchene L, Kuhnel R, Stilp E, Reyes E, Remhof A, Hagemann H and Battaglia C 2017 A stable 3 V all-solid-state sodium-ion battery based on a closo-borate electrolyte *Energy Environ. Sci.* **10** 2609–15

[135] Tang W S, Yoshida K, Soloninin A V, Skoryunov R V, Babanova O A, Skripov A V, Dimitrievska M, Stavila V, Orimo S and Udovic T J 2016 Stabilizing superionic-conducting structures via mixed-anion solid solutions of monocarba-closo-borate salts *ACS Energy Lett.* **1** 659–64

[136] Andersson M *et al* 2021 Promoting persistent superionic conductivity in sodium monocarba-closo-dodecaborate $NaCB_{11}H_{12}$ via confinement within nanoporous silica *J. Phys. Chem.* C **125** 16689–99

[137] Lu Z and Ciucci F 2016 Structural origin of the superionic Na conduction in Na2B10H10 closo-borates and enhanced conductivity by Na deficiency for high performance solid electrolytes *J. Mater. Chem.* A **4** 17740–8

[138] Sau K, Ikeshoji T, Kim S, Takagi S and Orimo S 2021 Comparative molecular dynamics study of the roles of anion-cation and cation-cation correlation in cation diffusion in $Li_2B_{12}H_{12}$ and $LiCB_{11}H_{12}$ *Chem. Mater.* **33** 2357–69

[139] Sau K, Ikeshoji T, Kim S, Takagi S, Akagi K and Orimo S 2019 Reorientational motion and Li^+-ion transport in $Li_2B_{12}H_{12}$ system: molecular dynamics study *Phys. Rev. Mater.* **3** 075402

[140] Varley J, Kweon K, Mehta P, Shea P, Heo T, Udovic T, Stavila V and Wood B 2017 Understanding ionic conductivity trends in polyborane solid electrolytes from *ab initio* molecular dynamics *ACS Energy Lett.* **2** 250–5

[141] Wood B C *et al* 2021 Paradigms of frustration in superionic solid electrolytes in press *Phil. Trans. R. Soc.* A **379** 20190467

[142] Wilmer D, Feldmann H and Lechner R 2002 Ion dynamics in solid solutions of sodium phosphate and sodium sulfate *Phys. Chem. Chem. Phys.* **4** 3260–5

[143] Soloninin A V, Dimitrievska M, Skoryunov R V, Babanova O A, Skripov A V, Tang W S, Stavila V, Orimo S and Udovic T J 2017 Comparison of anion reorientational dynamics in MCB_9H_{10} and $M_2B_{10}H_{10}$ (M = Li, Na) via nuclear magnetic resonance and quasielastic neutron scattering studies *J. Phys. Chem.* C **121** 1000–12

[144] Skripov A, Soloninin A, Ley M, Jensen T and Filinchuk Y 2013 Nuclear magnetic resonance studies of BH4 reorientations and Li diffusion in $LiLa(BH_4)_3Cl$ *J. Phys. Chem.* C **117** 14965–72

[145] Payandeh S, Brighi M, Sadikin Y, Ravnsbæk D B, Černý R, Skibsted J and Jensen T R 2017 Synthesis, structure, and Li-ion conductivity of $LiLa(BH_4)_3X$, X = Cl, Br, I *J. Phys. Chem.* C **121** 19010–21

[146] Lefevr J, Cervini L, Griffin J M and Blanchard D 2018 Lithium conductivity and ions dynamics in $LiBH_4/SiO_2$Solid-electrolytes studied by solid-state NMR and quasi elastic neutron scattering and applied in lithium-sulfur batteries *J. Phys. Chem.* C **122** 15264–75

[147] Santos J, Simon P, Bernot A, Babasi C, Ward P, Hwang S, Zidan R and Teprovich J 2021 Synergistic effect of nanoionic destabilization and partial dehydrogenation for enhanced ionic conductivity in MBH_4-C_{60} (M = Li^+, Na^+) nanocomposites *J. Solid. State Electrochem.* **25** 1441–52

[148] Mohtadi R, Tutusaus O, Arthur T S, Zhao-Karger Z and Fichtner M 2021 The metamorphosis of rechargeable magnesium batteries *Joule* **5** 581–617

[149] Mohtadi R, Matsui M, Arthur T S and Hwang S J 2012 Magnesium borohydride: from hydrogen storage to magnesium battery *Angew. Chem., Int. Ed.* **51** 9780–3

[150] Tutusaus O, Mohtadi R, Arthur T S, Mizuno F, Nelson E G and Sevryugina Y V 2015 An Efficient Halogen-Free Electrolyte for Use in Rechargeable Magnesium Batteries *Angew. Chem. Int. Ed.* **54** 7900–4

[151] Kar M, Tutusaus O, MacFarlane D R and Mohtadi R 2019 Novel and versatile room temperature ionic liquids for energy storage *Energy Environ. Sci.* **12** 566–71

[152] Dong H, Tutusaus O, Liang Y, Zhang Y, Lebens-Higgins Z, Yang W, Mohtadi R and Yao Y 2020 High-power Mg batteries enabled by heterogeneous enolization redox chemistry and weakly coordinating electrolytes *Nat. Energy* **5** 1043–50

[153] Roedern E, Kühnel R S, Remhof A and Battaglia C 2017 Magnesium ethylenediamine borohydride as solid-state electrolyte for magnesium batteries *Sci. Rep.* **7** 2–7

[154] Yan Y *et al* 2020 The mechanism of Mg^{2+} conduction in ammine magnesium borohydride promoted by a neutral molecule *Phys. Chem. Chem. Phys.* **22** 9204–9

[155] Yan Y, Grinderslev J B, Jørgensen M, Skov L N, Skibsted J and Jensen T R 2020 Ammine magnesium borohydride nanocomposites for all-solid-state magnesium batteries *ACS Appl. Energy Mater.* **3** 9264–70

[156] Le Ruyet R, Berthelot R, Salager E, Florian P, Fleutot B and Janot R 2019 Investigation of $Mg(BH_4)(NH_2)$-based composite materials with enhanced Mg^{2+} ionic conductivity *J. Phys. Chem.* C **123** 10756–63

[157] Mizuno F, Mohtadi R, Tutusaus O, Fichtner M and Zhao-Karger Z 2017 Solid-phase magnesium boranyl electrolytes for a magnesium battery *US009716289B1*

[158] Burankova T, Roedern E, Maniadaki A E, Hagemann H, Rentsch D, Lodziana Z, Battaglia C, Remhof A and Embs J P 2018 Dynamics of the coordination complexes in a solid-state Mg electrolyte *J. Phys. Chem. Lett.* **9** 6450–5

[159] Kisu K, Kim S, Shinohara T, Zhao K, Züttel A and Orimo S 2021 Monocarborane cluster as a stable fluorine-free calcium battery electrolyte *Sci. Rep.* **11** 7563

[160] Higashi S, Miwa K, Aoki M and Takechi K 2014 A novel inorganic solid state ion conductor for rechargeable Mg batteries *Chem. Commun.* **50** 1320–2

[161] Kisu K, Kim S, Inukai M, Oguchi H, Takagi S and Orimo S 2020 Magnesium borohydride ammonia borane as a magnesium ionic conductor *ACS Appl. Energy Mater.* **3** 3174–9

[162] Chen X, Yuan F, Gu Q and Yu X 2013 Synthesis, structures and hydrogen storage properties of two new H-enriched compounds: $Mg(BH4)_2(NH_3BH_3)_2$ and $Mg(BH_4)_2\cdot(NH_3)_2(NH_3BH_3)$ *Dalton Trans.* **42** 14365–8

[163] Jepsen L H, Ban V, Møller K T, Lee Y S, Cho Y W, Besenbacher F, Filinchuk Y, Skibsted J and Jensen T R 2014 Synthesis, crystal structure, thermal decomposition, and 11B MAS NMR characterization of Mg(BH4)2(NH3BH 3)2 *J. Phys. Chem.* C **118** 12141–53

[164] Le Ruyet R, Fleutot B, Berthelot R, Benabed Y, Hautier G, Filinchuk Y and Janot R 2020 $Mg_3(BH_4)_4(NH_2)_2$as inorganic solid electrolyte with high Mg^{2+}ionic conductivity *ACS Appl. Energy Mater.* **3** 6093–7

[165] Liu X-R, Chen X-M, Zhang J, Jensen T R and Chen X 2019 The interconversion between THF·B_3H_7 and $B_3H_8{}^-$: an efficient synthetic method for MB3H8 (M = Li and Na) *Dalton Trans.* **48** 5140–3

[166] Andersson M S, Grinderslev J B, Chen X-M, Chen X, Häussermann U, Zhou W, Jensen T R, Karlsson M and Udovic T J 2021 Interplay between the reorientational dynamics of the $B_3H_8{}^-$ anion and the structure in KB_3H_8 *J. Phys. Chem.* C **125** 3716–24

[167] Sadikin Y, Skoryunov R V, Babanova O A, Soloninin A V, Lodziana Z, Brighi M, Skripov A V and Černý R 2017 Anion disorder in K3BH4B12H12 and its effect on cation mobility *J. Phys. Chem.* C **121** 5503–14

[168] Paskevicius M, Hansen B R S, Jørgensen M, Richter B and Jensen T R 2017 Multifunctionality of silver closo-boranes *Nat. Commun.* **8** 10–15

[169] Gradišek A, Jørgensen M, Paskevicius M, Hansen B R S and Jensen T R 2021 Molecular dynamics in $Ag_2B_{12}H_{12}$ studied by nuclear magnetic resonance *J. Phys. Chem.* C **125** 5534–41

[170] Jørgensen M, Lee Y S, Paskevicius M, Hansen B R S and Jensen T R 2021 Synthesis and crystal structures of decahydro-closo-decaborates of the divalent cations of strontium and manganese *J. Solid State Chem.* **298** 4–12

[171] Jørgensen M, Zhou W, Wu H, Udovic T J, Paskevicius M, Černý R and Jensen T R 2021 Polymorphism of calcium decahydrido-closo-decaborate and characterization of its hydrates *Inorg. Chem.* **60** 10943–57

[172] Lee W, Tamura S and Imanaka N 2017 New calcium ion conducting solid electrolyte with NASICON-type structure *Chem. Lett.* **46** 1486–9

[173] Ozolins V, Majzoub E H and Wolverton C 2008 First-principles prediction of a ground state crystal structure of magnesium borohydride *Phys. Rev. Lett.* **100** 135501

[174] Voss J, Hummelshøj J S, Łodziana Z and Vegge T 2009 Structural stability and decomposition of $Mg(BH_4)_2$ isomorphs—an *ab initio* free energy study *J. Phys.: Condens. Matter* **21** 012203

[175] Zhou X-F, Oganov A R, Qian G-R and Zhu Q 2012 First-principles determination of the structure of magnesium borohydride *Phys. Rev. Lett.* **109** 245503

[176] Heere M, Hansen A L, Payandeh S H, Aslan N, Gizer G, Sørby M H, Hauback B C, Pistidda C, Dornheim M and Lohstroh W 2020 Dynamics of porous and amorphous magnesium borohydride to understand solid state Mg-ion-conductors *Sci. Rep.* **10** 1–11

[177] Silvi L, Zhao-Karger Z, Röhm E, Fichtner M, Petry W and Lohstroh W 2019 A quasielastic and inelastic neutron scattering study of the alkaline and alkaline-earth borohydrides $LiBH_4$ and $Mg(BH_4)_2$ and the mixture $LiBH_4 + Mg(BH_4)_2$ *Phys. Chem. Chem. Phys.* **21** 718–28

[178] Silvi L, Röhm E, Fichtner M, Petry W and Lohstroh W 2016 Hydrogen dynamics in β-Mg(BH4)2 on the picosecond timescale *Phys. Chem. Chem. Phys.* **18** 14323–32

[179] Blanchard D *et al* 2012 Hindered rotational energy barriers of BH_4—tetrahedra in β-$Mg(BH4)_2$ from quasielastic neutron scattering and DFT calculations *J. Phys. Chem.* C **116** 2013–23

[180] Jansen M 1991 Volume effect or paddle-wheel mechanism—fast alkali-metal ionic conduction in solids with rotationally disordered complex anions *Angew. Chem., Int. Ed. Engl.* **30** 1547–58

[181] Solovev M V, Chashchikhin O V, Dorovatovskii P V, Khrustalev V N, Zyubin A S, Zyubina T S, Kravchenko O V, Zaytsev A A and Dobrovolsky Y A 2018 Hydrolysis of $Mg(BH_4)_2$ and its coordination compounds as a way to obtain hydrogen *J. Power Sources* **377** 93–102

[182] Kisu K, Kim S, Yoshida R, Oguchi H, Toyama N and Orimo S 2020 Microstructural analyses of all-solid-state Li–S batteries using $LiBH_4$-based solid electrolyte for prolonged cycle performance *J. Energy Chem.* **50** 424–9

[183] Dao H A, López-Aranguren P, Zhang J, Cuevas F and Latroche M 2020 Solid-state Li-ion batteries operating at room temperature using new borohydride argyrodite electrolytes *Materials* **13** 4028

[184] Kim S, Harada K, Toyama N, Oguchi H, Kisu K and Orimo S 2020 Room temperature operation of all-solid-state battery using a closo-type complex hydride solid electrolyte and a $LiCoO_2$ cathode by interfacial modification *J. Energy Chem.* **43** 47–51

[185] Attias R, Salama M, Hirsch B, Pant R, Gofer Y and Aurbach D 2019 Anion effects on cathode electrochemical activity in rechargeable magnesium batteries: a case study of V_2O_5 *ACS Energy Lett.* **4** 209–14

[186] Wan L F, Perdue B R, Apblett C A and Prendergast D 2015 Mg desolvation and intercalation mechanism at the Mo_6S_8 chevrel phase surface *Chem. Mater.* **27** 5932–40

[187] Wang D, Gao X, Chen Y, Jin L, Kuss C and Bruce P G 2018 Plating and stripping calcium in an organic electrolyte *Nat. Mater.* **17** 16–20

[188] Jie Y, Tan Y, Li L, Han Y, Xu S, Zhao Z, Cao R, Ren X, Huang F and Lei Z 2020 Electrolyte solvation manipulation enables unprecedented room-temperature calcium-metal batteries *Angew. Chem., Int. Ed.* **59** 12689–93

[189] Meng T, Young K-H, Wong D F and Nei J 2017 Ionic liquid-based non-aqueous electrolytes for nickel/metal hydride batteries *Batteries* **3** 4

[190] Uesato H, Miyaoka H, Ichikawa T and Kojima Y 2019 Hybrid nickel-metal hydride/hydrogen battery *Int. J. Hydrog. Energy* **44** 4263–70

[191] Berger A, Buckley C E and Paskevicius M 2021 Synthesis of closo-$CB_{11}H_{12}$—salts using common laboratory reagents *Inorg. Chem.* **60** 14744–51

[192] Moury R, Gigante A and Hagemann H 2017 An alternative approach to the synthesis of NaB3H8 and Na2B12H12 for solid electrolyte applications *Int. J. Hydrog. Energy* **42** 22417–21

[193] Toom L, Kütt A and Leito I 2019 Simple and scalable synthesis of the carborane anion $CB_{11}H_{12}$ *Dalton Trans.* **48** 7499–502

[194] Zhu M, Pang Y, Lu F, Shi X, Yang J and Zheng S 2019 *In situ* formed Li–B–H complex with high Li-ion conductivity as a potential solid electrolyte for Li batteries *ACS Appl. Mater. Interfaces* **11** 14136–41

[195] Paskevicius M, Jepsen L H, Schouwink P, Černý R, Ravnsbæk D B, Filinchuk Y, Dornheim M, Besenbacher F and Jensen T R 2017 Metal borohydrides and derivatives—synthesis, structure and properties *Chem. Soc. Rev.* **46** 1565–634

[196] Grinderslev J B, Lee Y, Paskevicius M, Møller K T, Yan Y, Cho Y W and Jensen T R 2020 Ammonium–ammonia complexes, $N_2H_7{}^+$, in ammonium closo-borate ammines: synthesis, structure, and properties *Inorg. Chem.* **59** 11449–58

[197] Andersson M S, Grinderslev J B, Jensen T R, García Sakai V, Häussermann U, Udovic T J and Karlsson M 2020 Interplay of $NH_4{}^+$ and $BH_4{}^-$ reorientational dynamics in NH_4BH_4 *Phys. Rev. Mater.* **4** 085002

[198] Grinderslev J B, Jepsen L H, Lee Y-S, Møller K T, Cho Y W, Černý R and Jensen T R 2020 Structural diversity and trends in properties of an array of hydrogen-rich ammonium metal borohydrides *Inorg. Chem.* **59** 12733–47

[199] Filippov S, Grinderslev J B, Andersson M S, Armstrong J, Karlsson M, Jensen T R, Klarbring J, Simak S I and Häussermann U 2019 Analysis of dihydrogen bonding in ammonium borohydride *J. Phys. Chem.* C **123** 28631–9